Check for updates

JGR Earth Surface

RESEARCH ARTICLE
10.1029/2023JF007254

Mapping Variations in Bedrock Weathering With Slope Aspect Under a Sedimentary Ridge-Valley System Using Near-Surface Geophysics and Drilling

Berit M. Hudson Rasmussen[1], Mong-Han Huang[1], W. Jesse Hahm[2], Daniella M. Rempe[3], David Dralle[4], and Mariel D. Nelson[3]

[1]Department of Geology, University of Maryland, College Park, MD, USA, [2]Department of Geography, Simon Fraser University, Burnaby, BC, Canada, [3]Department of Geosciences, Jackson School of Geosciences, The University of Texas at Austin, Austin, TX, USA, [4]Pacific Southwest Research Station, United States Forest Service, Albany, CA, USA

Key Points:

- A combination of geophysics and borehole measurements allows us to characterize lateral critical zone structure in a ridge-channel system
- Despite a strong aspect-dependent contrast in soil thickness, saprolite thickness does not vary with slope aspect
- Rock physics modeling using seismic velocity suggests that inherited bedrock fractures substantially contribute to saprolite total porosity

Supporting Information:

Supporting Information may be found in the online version of this article.

Correspondence to:

M.-H. Huang,
mhhuang@umd.edu

Citation:

Hudson Rasmussen, B. M., Huang, M.-H., Hahm, W. J., Rempe, D. M., Dralle, D., & Nelson, M. D. (2023). Mapping variations in bedrock weathering with slope aspect under a sedimentary ridge-valley system using near-surface geophysics and drilling. *Journal of Geophysical Research: Earth Surface*, *128*, e2023JF007254. https://doi.org/10.1029/2023JF007254

Received 14 MAY 2023
Accepted 19 JUN 2023

Author Contributions:

Conceptualization: Berit M. Hudson Rasmussen, Mong-Han Huang, Daniella M. Rempe
Data curation: Berit M. Hudson Rasmussen, Mong-Han Huang, Mariel D. Nelson
Formal analysis: Berit M. Hudson Rasmussen, Mong-Han Huang
Funding acquisition: Mong-Han Huang
Investigation: Berit M. Hudson Rasmussen, Mong-Han Huang

© 2023 The Authors.
This is an open access article under the terms of the Creative Commons Attribution-NonCommercial License, which permits use, distribution and reproduction in any medium, provided the original work is properly cited and is not used for commercial purposes.

Abstract Understanding how soil thickness and bedrock weathering vary across ridge and valley topography is needed to constrain the flowpaths of water and sediment production within a landscape. Here, we investigate saprolite and weathered bedrock properties across a ridge-valley system in the Northern California Coast Ranges, USA, where topography varies with slope aspect such that north-facing slopes have thicker soils and are more densely vegetated than south-facing slopes. We use active source seismic refraction surveys to extend observations made in boreholes to the hillslope scale. Seismic velocity models across several ridges capture a high velocity gradient zone (from 1,000 to 2,500 m/s) located ~4–13 m below ridgetops that coincides with transitions in material strength and chemical depletion observed in boreholes. Comparing this transition depth across multiple north- and south-facing slopes, we find that the thickness of saprolite does not vary with slope aspects. Additionally, seismic survey lines perpendicular and parallel to bedding planes reveal weathering profiles that thicken upslope and taper downslope to channels. Using a rock physics model incorporating seismic velocity, we estimate the total porosity of the saprolite and find that inherited fractures contribute a substantial amount of pore space in the upper 6 m, and the lateral porosity structure varies strongly with hillslope position. The aspect-independent weathering structure suggests that the contemporary critical zone structure at Rancho Venada is a legacy of past climate and vegetation conditions.

Plain Language Summary Below Earth's ground surface, porous space within weathered bedrock can store a significant amount of water, which is essential for ecosystems, particularly during the growing seasons. Collecting hydrologic data and core samplings from boreholes provides direct measurements about how bedrock is weathered and broken down toward the earth surface. Our study site is located in a series of ridges and valleys in Northern California, USA, where the local Mediterranean climate has distinctive dry summers and wet winters. This site represents a common topography along the east side of the Coast Ranges. In addition to synthesizing borehole and hydrologic data, we conduct complementary seismic refraction surveys to image material strength in the subsurface in 2D. These images can better capture the lateral variation of weathering zone thickness from channels to ridgetops. Seismic velocity derived from seismic refraction data shows an increase of material strength at the transition zone between saprolite and bedrock that agrees with borehole observations. Although vegetation density is much higher in the north- than the south-facing hills, the depth to fresh bedrock is roughly the same. Our results also indicate that porous spaces in the weathered bedrock have the potential to store more water than annual precipitation.

1. Introduction

The transformation of fresh bedrock into weathered bedrock and mobile soil in the subsurface critical zone is facilitated by changes in chemical composition, material strength, and porosity with depth. These processes dictate how landscapes store and release water to trees and streams (Brooks et al., 2015). Documenting the structure of the critical zone, including the thickness and subsurface topography of different materials, is therefore crucial to quantifying water storage (Callahan et al., 2020; Flinchum, Holbrook, Rempe, et al., 2018; Rempe & Dietrich, 2014) and predicting ecosystem and landscape response to climate change (Callahan et al., 2022; Godderis & Brantley, 2013; Sullivan et al., 2022). Water storage dynamics are not homogenous at the hillslope scale but are influenced by microtopography (Wang et al., 2021), elevation (Klos et al., 2018; Nielsen et al., 2021),

21699011, 2023, 7, Downloaded from https://agupubs.onlinelibrary.wiley.com/doi/10.1029/2023JF007254 by Test, Wiley Online Library on [03/07/2023]. See the Terms and Conditions (https://onlinelibrary.wiley.com/terms-and-conditions) on Wiley Online Library for rules of use; OA articles are governed by the applicable Creative Commons License

Methodology: Berit M. Hudson Rasmussen, Mong-Han Huang, W. Jesse Hahm
Resources: Berit M. Hudson Rasmussen, Mong-Han Huang, W. Jesse Hahm, Daniella M. Rempe, David Dralle
Software: Berit M. Hudson Rasmussen, Mong-Han Huang
Supervision: Mong-Han Huang
Validation: Berit M. Hudson Rasmussen, Mong-Han Huang
Visualization: Berit M. Hudson Rasmussen, Mong-Han Huang
Writing – original draft: Berit M. Hudson Rasmussen, Mong-Han Huang
Writing – review & editing: Berit M. Hudson Rasmussen, Mong-Han Huang, W. Jesse Hahm, Daniella M. Rempe, Mariel D. Nelson

and slope aspect (Anderson et al., 2014). Critical zone structure can additionally be modulated by lithology (Hahm et al., 2014; Leone et al., 2020) and climate (Anderson et al., 2019; Inbar et al., 2018). Exploration of the spatially variable hydrologic dynamics of a landscape therefore requires characterization of subsurface structure over broad spatial scales, and in different geologic settings.

Many studies have observed that with increased solar radiation on equator-facing hillslopes at mid-high latitudes, separate microclimates can be found on equator-facing (i.e., south-facing, in the northern hemisphere) versus pole-facing (i.e., north-facing) hillslopes (Pelletier et al., 2018). In presently precipitation-limited environments (as opposed to temperature-limited), north-facing slopes of the northern hemisphere tend to have more vegetation, and thicker, wetter soils, while south-facing slopes are drier and less vegetated with thinner soils (Pelletier et al., 2018). While surface slope, tree density, and soil thickness have been well documented to vary based on aspect dependency (Bale et al., 1998; Inbar et al., 2018), fewer studies address the influence of aspect dependency and climate on deeper weathering transitions. Those that do focus primarily on snow-dominated systems or granite lithology (Anderson et al., 2013, 2014; Leone et al., 2020; Nielsen et al., 2021).

Seismic refraction can effectively capture the heterogeneity in the subsurface weathered bedrock structure, which can vary drastically from ridge to channel (Leone et al., 2020; Pasquet et al., 2022; Wang et al., 2021). By combining borehole and geophysical methods, recent studies have calibrated geophysical data to direct observations to infer weathering thickness across a landscape (Flinchum, Holbrook, Rempe, et al., 2018; Gu et al., 2020; Hayes et al., 2019; Holbrook et al., 2014, 2019; Olona et al., 2010). This combined approach allows for better modeling of subsurface water flow dynamics (Gu et al., 2020), comparison of slope aspect microclimates (Leone et al., 2020), and rock physics modeling of porosity (Callahan et al., 2020; Grana et al., 2022; Gu et al., 2020; Hayes et al., 2019; Holbrook et al., 2014). These studies are important advances and have helped to test and calibrate models of critical zone evolution, but they have documented only a fraction of the diverse combinations of topography, biota, lithology, and climate present across Earth's terrestrial surface.

In this study, we image critical zone structure through active-source seismic refraction surveys across a series of sedimentary ridges and valleys in the Mediterranean climate of the California Coast Ranges, USA. The site, Rancho Venada, is an ideal location to explore critical zone processes given its consistent bedding orientation, lack of complicating deformation features, and striking contrast in vegetation density with slope aspect. Sedimentary lithologies are understudied in critical zone literature, the vast majority of which involve granite, and Rancho Venada therefore provides a setting to examine the influence of bedding planes and interbedded lithology on subsurface structure. Characterizing water storage dynamics in this setting is essential as Rancho Venada faces increased drought frequency (East & Sankey, 2020) and rainfall-triggered landslides (Handwerger et al., 2019; Nelson et al., 2017; Sanders et al., 2019). A 2018 drilling campaign established weathered material extending 11–17 m below ridgetops, and only 1–2 m below channels. Building on this previous work, we ask (a) How does weathering, as expressed by bedrock fracturing and chemical alteration, vary with hillslope aspect? (b) What is the role of sedimentary bedding orientation in a critical zone structure? (c) What is the water storage capacity of the weathered bedrock and how does this vary across the landscape? To respond to these questions, we perform a comprehensive comparison of seismic velocity with physical, chemical, and hydrologic properties measured through borehole analysis by Pedrazas et al. (2021) and Hahm et al. (2022).

2. Field Site

2.1. Geologic Setting

The study site, Rancho Venada, is located 16 km west of Williams, California, USA, on the western border of the Sacramento Valley, and is lined with hills organized parallel to the strike of east-dipping turbidite beds (Figure 1). We focus on a ridge dissected by evenly spaced (~100–150 m) channels. The specific hills included in this study—referred to as MH2R, MH3R, and MH7R—are underlain by late Cretaceous bedrock of the Great Valley Sequence, composed primarily of thinly interbedded mudstone and siltstone, and capped with sandstone (Figure 1; Rich, 1971; Pedrazas et al., 2021). These units are separated from the deformed metamorphic Franciscan Complex by the Stony Creek Fault Zone to the west (Rich, 1971). Originally uplifted and tilted due to the subduction of the Farallon Plate below the North American Plate, Rancho Venada has been experiencing general northwest-southeast compression for the past 3–5 Ma (Atwater & Stock, 1998). There are no major faults or folds within these ridges, with only cm-to-meter-scale structures (monocline fold) observed (Harwood & Helley, 1987;

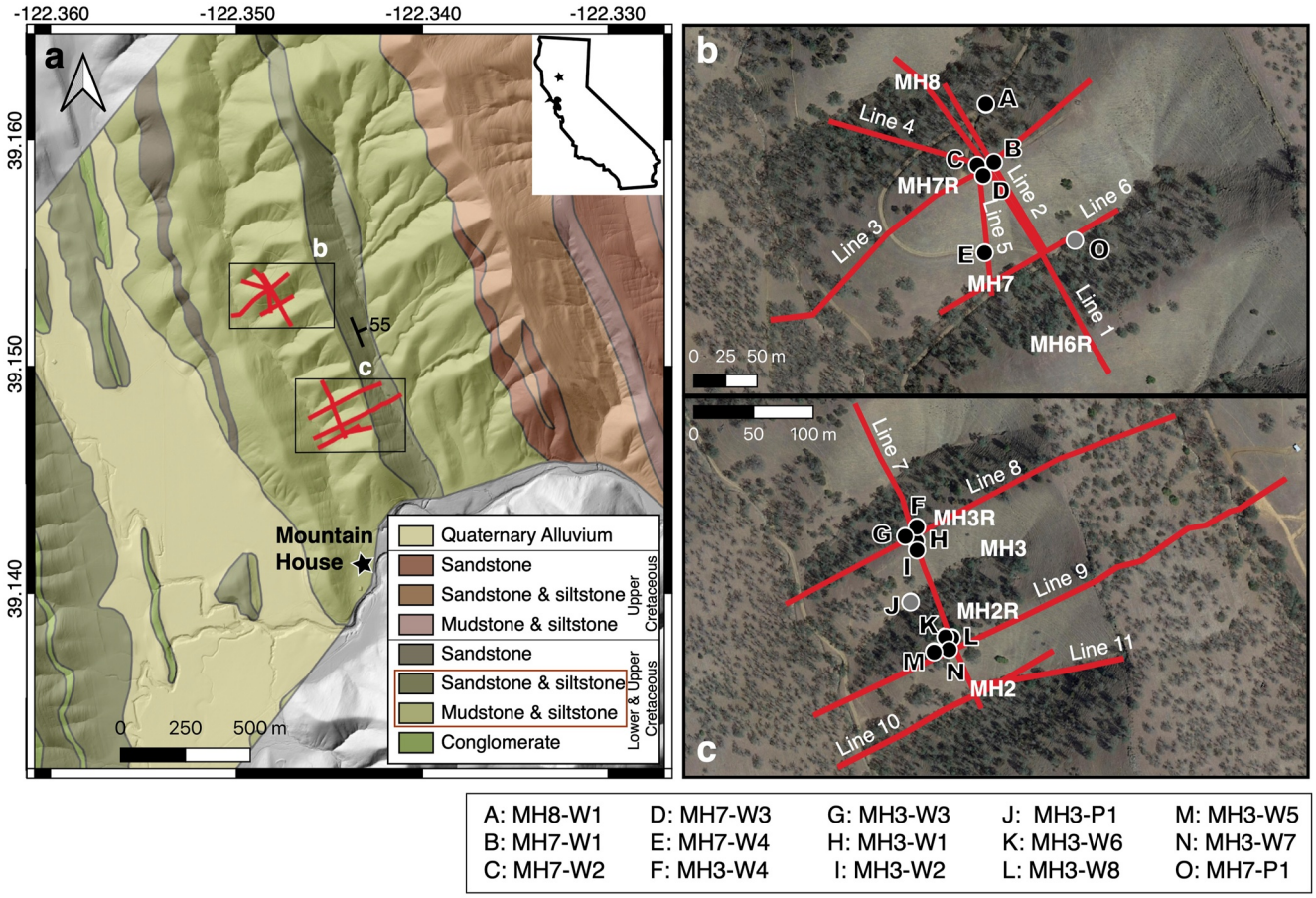

Figure 1. Geologic map of the study location near Williams, California, USA (after Rich, 1971 and Nelson et al., 2017). The geologic units underlying our study hills are outlined in the red box in the legend. The black star in the inset map indicates the study site Rancho Venada. Insets b and c show the locations of the specific hills of interest and the contrasting tree density on north- and south-facing slopes. For the naming convention, MH2 represents the second channel from south, and MH2R represents the ridgetop north of the second watershed. Red lines represent seismic survey lines 1–10. Black circles indicate locations of boreholes cored using a drill-rig, while gray circles were drilled using a Shaw backpack drill (Pedrazas et al., 2021). Letters A to O indicate the borehole number.

Rich, 1971). The hills were formed at least ~1–2 Ma based on a channel incision rate of ~0.1 mm/yr (Pedrazas et al., 2021). The regional climate is sub-humid with pronounced wet and dry seasons and a mean precipitation of 534 mm/yr (Hahm et al., 2022). Vegetation is primarily grassland and Blue oak-manzanita woodland, with a notable lack of trees on the south-facing hillslopes and a higher vegetation density on the north-facing hillslopes (see Figures 1b and 1c).

2.2. Previous Studies

Fourteen boreholes were drilled along three hills at Rancho Venada in November 2018 (Pedrazas et al., 2021). Three deep boreholes were drilled to the total relief of the hills: 47, 20, and 20 m for MH7R, MH3R, and MH2R, respectively. In this study, MH7 refers to the seventh channel north of the Mountain House (MH), and *R* refers to the ridgetop north of the channel. The drilling process involved augering, coring, and standard penetration tests to obtain blowcount rate (ASTM, 2022; Pedrazas et al., 2021). Blowcount rate is the number of blows necessary to advance a hollow core tube 6 inches into the ground, providing a measure of material strength. Shallower boreholes were augered to 6–9 m depth or drilled with a Shaw drill to <2 m in the channels. All boreholes were sampled for elemental composition, and images were produced using an optical borehole imager (OBI) for each of the three deep boreholes to capture fracture and bedding density and orientation as well as color. Yellowness hue was calculated from these images as a proxy for chemical weathering (following Holbrook et al., 2019). Matrix porosity was calculated from auger chips and pieces of the core using the Accupyc Gas Pycnometer and GeoPyc Envelope Density Analyzer. Neutron count measurements were taken every foot by lowering the probe

21699011, 2023, 7, Downloaded from https://agupubs.onlinelibrary.wiley.com/doi/10.1029/2023JF007254 by Test, Wiley Online Library on [03/07/2023]. See the Terms and Conditions (https://onlinelibrary.wiley.com/terms-and-conditions) on Wiley Online Library for rules of use; OA articles are governed by the applicable Creative Commons License

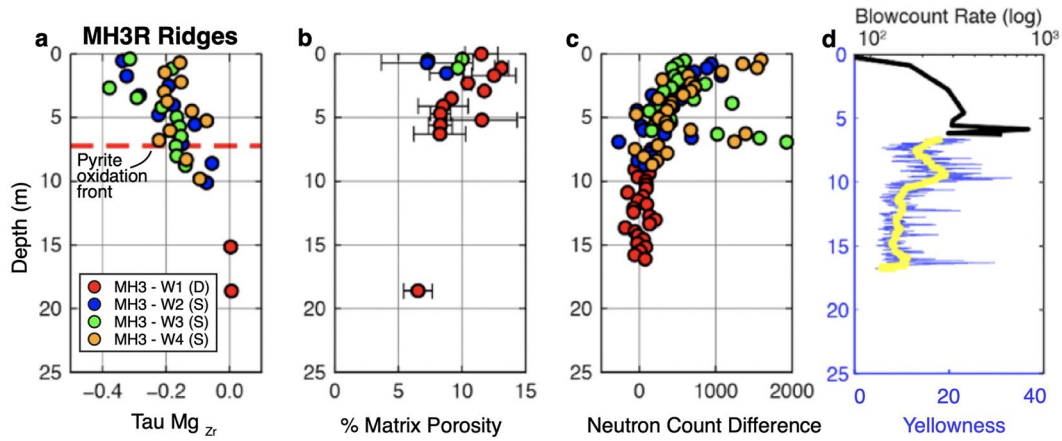

Figure 2. Borehole data for the MH3R ridgetop (see Figure 1 for location). Data are from Pedrazas et al. (2021) and excludes data below 25 m from MH3-W1. (a) Depletion of magnesium with depth relative to the parent material, with zirconium as the immobile element. It indicates the depletion of magnesium (a), sodium, and potassium toward the surface. Here we chose τ_{Mg} because it shows the most obvious depletion toward the surface. Other τ values are detailed in Pedrazas et al. (2021). The pyrite oxidation depth (from sulfur) shown as the red dashed line at 6.3 m. D and S represent deep and shallow boreholes, respectively. (b) Matrix porosity, (c) neutron count difference, highlighting where moisture storage in the borehole is variable, and (d) log blowcount rate on the upper *x*-axis. Yellowness hue (blue line) is shown on the lower *x*-axis. The yellow line represents the smoothed yellowness hue.

down each borehole until it reached the water table. These measurements were repeated every month over the course of 2 years to measure the relative seasonal water storage with depth (Hahm et al., 2022; Figures 2c–2f). Drilling logistics and borehole measurements are described in detail in Pedrazas et al. (2021).

Borehole analysis highlighted three interfaces across the hillslopes: *Interface 1* as the soil—pervasively fractured material transition (i.e., soil to saprolite), *Interface 2* as the pervasively fractured—discretely fractured rock transition (i.e., saprolite to weathered bedrock), and *Interface 3* as the discretely—rarely fractured rock transition (i.e., weathered to fractured bedrock). Chemical analysis of the cores included using the mass transfer coefficient (τ), to track elemental changes as the parent material is weathered. The pyrite oxidation front is also observed at a 6–7 m depth for all boreholes (Figure 2a). Matrix porosity for all sites ranges from 15% to 20% near the surface and drops to 10% within 5 m, and even lower to 5% by 24 m (Pedrazas et al., 2021). The MH3R (Figure 2d) and MH7R ridges display a large jump in blowcount rate, indicating an increase in material strength, at a 6–7 m depth, while MH2R shows a more gradual increase in blowcount rate. Neutron probe counts indicate dynamic seasonal rock moisture storage to a depth of 8–9 m (Figure 2c). Pedrazas et al. (2021) therefore propose the Interface 2 (saprolite-weathered bedrock) transition depths (MH7R: 6.5 ± 0.8 m, MH3R: 6.3 ± 0.8 m, MH2R: 7.5 ± 1.6 m; Pedrazas et al., 2021) based on the sharp increase in blowcount rate and the pyrite weathering front observed in each borehole. The saprolite above Interface 2 shows depletion of Mg, Na, and K, higher porosity, substantial fracturing, and storage of seasonally variable rock moisture. Yellowness hue, an indicator of chemical weathering, drops abruptly at a 17.5, 11, and 10.5 m depth for MH7R, MH3R, and MH2R, respectively. Pedrazas et al. (2021) define the Interface 3 (weathered- fractured bedrock) transition at the above depths based on yellowness hue and further decrease in fracture density.

Hydrologic analysis by Hahm et al. (2022) utilized a combination of remotely sensed soil moisture and evapotranspiration data, downhole rock moisture surveys, and oak sapflow and water potential measurements to monitor seasonal water storage and vegetation dynamics at Rancho Venada. During two drought years, the winter wet season did not replenish the subsurface storage capacity enough to recharge groundwater, discharge water as streamflow, or sustain trees, which exhibited lower sapflow and smaller leaf size. Their results suggest that Rancho Venada has a large water-holding storage capacity relative to the precipitation it receives during meteorological droughts and is therefore precipitation-limited (in the sense of Hahm, Dralle, et al., 2019). Repeat downhole neutron probe measurements across the 2019–2021 water years characterized seasonal rock moisture dynamics, and estimated volumetric water content to vary between 25% and 40% throughout the year.

Huang et al. (2021) conducted a seismic survey parallel to the bedding strike along the MH2-MH4 catchments at Rancho Venada in December 2019. In this study, we examine the same seismic refraction result (Section 4.1.3)

21699011, 2023, 7, Downloaded from https://agupubs.onlinelibrary.wiley.com/doi/10.1029/2023JF007254 by Test, Wiley Online Library on [03/07/2023]. See the Terms and Conditions (https://onlinelibrary.wiley.com/terms-and-conditions) on Wiley Online Library for rules of use; OA articles are governed by the applicable Creative Commons License

in comparison with data from drilling and nine additional seismic surveys to understand the deep critical zone structure.

3. Methods

3.1. Seismic Refraction Surveys and Modeling

We conducted 11 active-source seismic refraction surveys: three lines oriented parallel to bedding (including one previously published bedding-parallel line, Line 7; Huang et al., 2021), six perpendicular to bedding, and two along the steepest descent of the north- and south-facing hillslopes (Figure 1). Parameters of the seismic surveys are shown in Table S1 in Supporting Information S1. We used 14-Hz geophones and created sources at a 3–10 m shot interval using 5–7 kg sledgehammers on a metal plate, which were recorded using the Geometrics ES-3000 system and Geoid systems. For all lines except Line 9, the shot interval was one m near borehole locations. We performed off-end shots 36–54 m away from the first geophone and after the last geophone for each survey. Locations along the seismic line were recorded with GPS to create an elevation profile of each seismic line using a digital elevation model (DEM) generated from an airborne lidar survey of Rancho Venada in 2017 (Dietrich, 2019).

We used the Geometrics PickWin software package to pick p-wave arrival times and the THB rj-MCMC inversion scheme from Huang et al. (2021) to generate seismic velocity models. For traditional inversion methods, smoothing is commonly used to regularize the inversion in order to reduce roughness coming from measurement errors. However, the smoothing parameter is normally set arbitrarily because the measurement error from p-wave picking is generally unknown. The THB rj-MCMC method uses a probabilistic model to estimate measurement uncertainty (called hyperparameter) and whether measurement uncertainty propagates with source-receiver distance. THB rj-MCMC produces a posterior distribution of an ensemble of velocity models that can fit the p-wave measurements equally well; therefore, we capture both the range of plausible solutions and the uncertainty associated with the model (Burdick & Lekic, 2017). The standard deviation of ensemble velocity can be calculated from the accepted models to indicate areas where the velocity has greater uncertainty (Huang et al., 2021). The THB method therefore allows for analysis of data uncertainty and explores model resolution along lateral distance and depth, which are important for assessing the reliability of seismic velocity images and interpretation of critical zone structure (Figure 3).

3.2. Borehole Comparison and Hillslope Analysis

To compare borehole data to seismic velocity measurements, we created a vertical velocity profile for each borehole located within 10 m of a seismic survey. We examined the p-wave velocity corresponding to the interface depth ranges from Table 1 of Pedrazas et al. (2021). Several boreholes were imaged by more than one seismic line and therefore have multiple recorded velocities. We averaged the velocity at each interface across all borehole-velocity profiles of the same survey line orientation. Since the interfaces are not abrupt boundaries, but transitional zones, we calculated the average velocity of the Interface 2 (saprolite to weathered bedrock transition) depth ± 1 standard deviation. Our result is a range of velocities over which we expect more rapid changes in material strength to occur. We then use this velocity zone to compare weathering structure across the three ridges. While borehole data is limited to one mid-slope location, we can calculate the depth to the bedding-parallel Interface 2 velocity range across the entire hillslope. We then compare the depth of this velocity range between north- and south-facing hillslopes to examine aspect differences in rock weathering. To account for different lengths of hillslopes, we divide horizontal distance and depth by the hillslope length to examine normalized profiles. We do the same process for Interface 3 (weathered to fractured bedrock transition).

3.3. Porosity Modeling

Matrix porosity (Φ_{matrix}) was measured from pieces of the core and reflects intra-grain pore space, ranging from >20% at the surface to <10% at a 10 m depth below ridges (Pedrazas et al., 2021). These measurements do not capture the total porosity which includes pore space associated with fractures, from processes such as gravity unloading and tectonic loading. On the other hand, seismic waves from near-surface active source seismic surveys are generally sensitive to length scale in 10 s of meters (e.g., Flinchum et al., 2022). In order to estimate a total

21699011, 2023, 7, Downloaded from https://agupubs.onlinelibrary.wiley.com/doi/10.1029/2023JF007254 by Test, Wiley Online Library on [03/07/2023]. See the Terms and Conditions (https://onlinelibrary.wiley.com/terms-and-conditions) on Wiley Online Library for rules of use; OA articles are governed by the applicable Creative Commons License

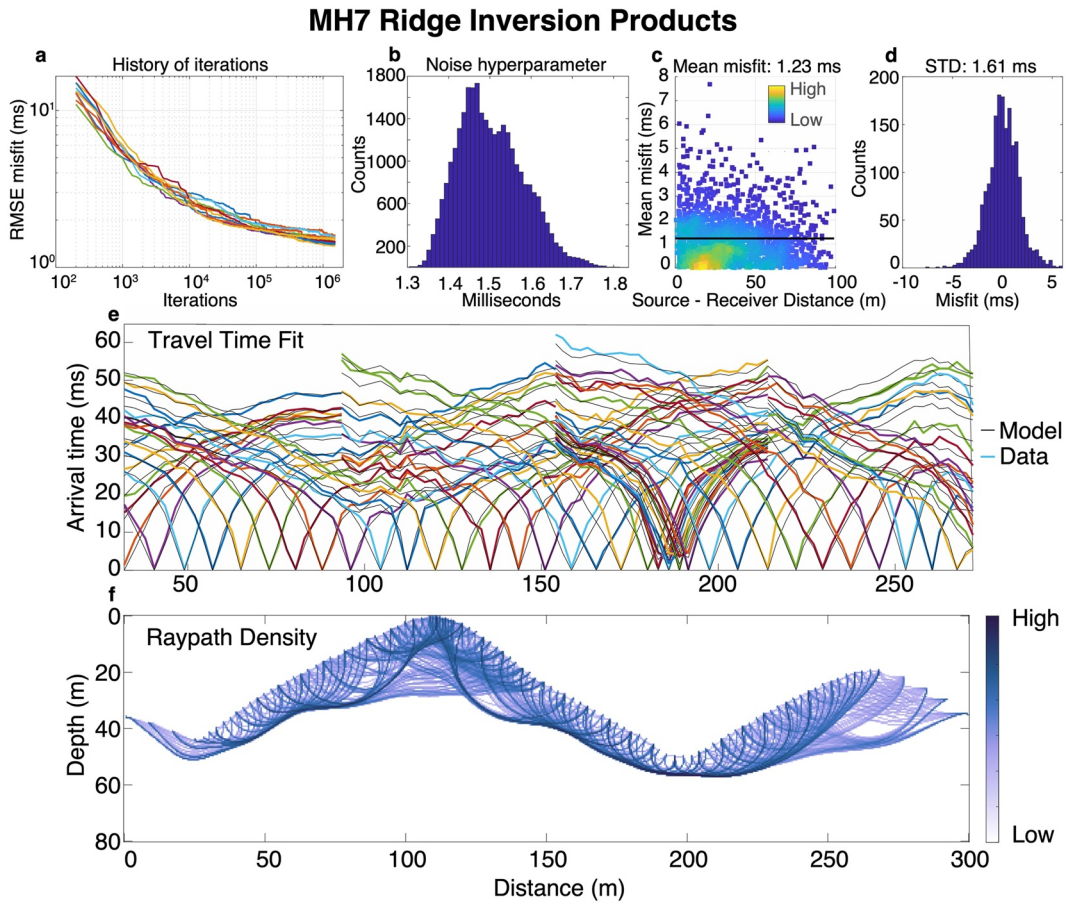

Figure 3. THB rj-MCMC products for Line 1. (a) RMSE misfit evolution in log-log scale. (b) Noise hyperparameter distribution after burn-in. (c) Mean misfit with source-receiver distance of the mean velocity model. (d) Standard deviation of the misfit in the mean velocity model. (e) Modeled travel time (black lines) and observed travel time (colored lines) of the mean velocity model. (f) Normalized raypath density of the mean velocity model.

bulk porosity (Φ_{total}) that is reflective of fracture and matrix pore space, and to obtain porosity values on a broader spatial scale, we apply a rock physics model to our seismic refraction data (e.g., Gu et al., 2020; Hayes et al., 2019; Holbrook et al., 2014). This model requires knowledge of the material mineralogy, relative saturation, and a set of empirical parameters related to grain size and other sediment properties. While we have elemental analysis of samples from the cores (Pedrazas et al., 2021), we do not know the exact mineral composition at Rancho Venada. We assumed three mineral components based on a geologic map of the region (Rich, 1971), and then varied the percentage of each, with quartz: 20%–50%, feldspar: 20%–30%, and chlorite: 20%–60%. This produces a range of bulk and shear moduli for the protolith. We then used the Hertz-Mindlin contact theory to calculate the dry bulk and shear modulus of the saprolite with shale or sandstone protolith, assuming a critical porosity of 0.4, contact points as 5, and an empirical parameter (e) as 5 (after Gu et al., 2020). Since saturation also contributes to the bulk modulus and we do not know relative saturation with depth, we vary water saturation between 0% and 100% and use Gasman's equation (Helgerud et al., 1999) to calculate the bulk and shear modulus of saprolite at different saturation states for each possible porosity value (see Table S2 in Supporting Information S1 for the mineral elastic moduli used in the model). With these bulk and shear moduli, we can then calculate seismic velocity using the following equation:

$$Vp = \sqrt{\frac{K_{sat} + \frac{4}{3}\mu_{sat}}{\rho_b}}, \quad (1)$$

where Vp, K_{sat}, μ_{sat}, and ρ_b are the seismic velocity, bulk modulus, shear modulus, and bulk density, respectively. We then compare Vp to the observed seismic velocity profile at each borehole. Since both bulk porosity and

21699011, 2023, 7, Downloaded from https://agupubs.onlinelibrary.wiley.com/doi/10.1029/2023JF007254 by Test, Wiley Online Library on [03/07/2023]. See the Terms and Conditions (https://onlinelibrary.wiley.com/terms-and-conditions) on Wiley Online Library for rules of use; OA articles are governed by the applicable Creative Commons License

21699011, 2023, 7, Downloaded from https://agupubs.onlinelibrary.wiley.com/doi/10.1029/2023JF007254 by Test, Wiley Online Library on [03/07/2023]. See the Terms and Conditions (https://onlinelibrary.wiley.com/terms-and-conditions) on Wiley Online Library for rules of use; OA articles are governed by the applicable Creative Commons License

relative saturation are unknown, the best-fitting velocities present a tradeoff curve between porosity and saturation, where any point along the curve predicts the same Vp. By assuming 0% saturation, we can make a 1D profile of porosity with depth.

While we do not have absolute measurements of relative water content with depth, we can estimate relative changes in volumetric water content with depth using repeat downhole neutron probe surveys previously conducted at Rancho Venada (Hahm et al., 2022). Repeated neutron probe surveys capture variations in moisture storage over time. By observing the change in water content ($\Delta\theta$) over multiple years, we can infer a minimum estimate of storage, and thus porosity, that is available at each depth. Porosity must be at least as high as $\Delta\theta$. For MH7R, we calculated $\Delta\theta$ from 02/12/2019 to 09/01/2021 using combined measurements from MH7-W2 and MH7-W3. We binned the measurements to 1 m depth intervals and calculated $\Delta\theta$ across the observation period after removing outliers. Wells MH3-W2, MH3-W3, and MH3-W4 were used for MH3R, and MH3-W6 and MH3-W7 were used for MH2R. The observation period for MH2R and MH3R was 11/15/2018 to 09/02/2021. Assuming that the matrix porosity is perennially saturated, then the seasonally dynamic rock moisture storage measured by the neutron probe represents additional porosity (e.g., from fractures), as opposed to porosity within the matrix (Φ_{matrix}). We can therefore estimate a minimum dynamic porosity ($\Phi_{dynamic}$) using,

$$\phi_{\text{dynamic}} = \Delta\theta + \phi_{\text{matrix}}, \tag{2}$$

that can be compared with the meter-scale modeled Φ_{total} from seismic refraction. $\Phi_{dynamic}$ represents a lower bound on Φ_{total}. Both $\Delta\theta$ and Φ_{matrix} were interpolated to 1 m depth intervals so they could be added together.

4. Results

4.1. Seismic Velocity Between Ridges and Channels

2D seismic images reveal changes in p-wave velocity (Vp) across the landscape. For all surveys, we mask out velocity past the ends of each line where no geophones are present. We additionally mask out regions where normalized smoothed raypath density is below 0.1 rays per model grid (using median filter with 5-pixel radius) and where the coefficient of variation (CoV; standard deviation divided by mean velocity) >30%. Low-velocity material is defined as Vp < 1,000 m/s, mid-velocity as 1,000 < Vp < 3,000 m/s, and high-velocity as Vp > 3,000 m/s. In this section, we report the results of Lines 1, 6, 7, and 8. The results of Line 2–5 and Lines 9–11 can be found in Supporting Information S1 (Figures S1, S2, S4, S5, S6, and Text S1). THB rj-MCMC provides information about the overall performance of the inversion (Figure 3). This includes the root mean square (RMSE) misfit of the predicted p-wave arrival times of each Markov Chain in different iterations (Figure 3a), a noise hyperparameter that can objectively estimate data uncertainty (Figure 3b), a model misfit distribution of the mean velocity model with different source-receiver distance, the standard deviation of that distribution (Figures 3c and 3d), the p-wave arrival time model fitting to data of the mean velocity model (Figure 3e), and a normalized raypath density distribution of the mean velocity model (Figure 3f). For example, for MH7, the RMSE misfit starts to stabilize after $\sim 5 \times 10^5$ iterations for all of the markov chains, implying that further iterations of model parameters do not further improve the fitting but instead can explore parameter distributions that can fit the data equally well (Huang et al., 2021). We find that the mean misfit of data (1.23 ms) is similar to the hyperparameter noise (~1.5 ms), suggesting a good balance of model parameters that do not under- or over-fit the data (Figures 3b and 3c).

4.1.1. MH7R Bedding-Parallel Transect (Line 1)

Below the ridgetop (MH7R), uncertainty is higher (CoV >30%) due to low raypath density. We therefore mask out much of the region and can only resolve 10 m below the ridgetop (Figures 3a, 3b, and 4b). Below the hillslopes, we can reliably resolve depths up to 20 m, while we can only resolve 10 m at the channels due to a rapid increase of seismic velocity. Three boreholes (MH7-W1, MH7-W2, and MH7-W3) at MH7R are within 10 m of Line 1 (Figure 1).

Below channels (MH7 and MH8), higher velocities are present at shallow depths, while toward the ridgetops, velocities <3,000 m/s extend for over 20 m (Figure 4a). The highest 2D velocity gradients occur below the channels, where velocity increases from 400 m/s to 4,000 m/s within 5 m (Figure 4c). A >300 m/s/m gradient contour zone can be traced across the hillslopes, suggesting a change in material strength within this high gradient zone. The 3,000 m/s contour line does not mirror the surface topography at the ridgetop. However, we do not have deep enough ray paths to constrain whether Vp > 3,000 m/s extends below the elevation of the channel

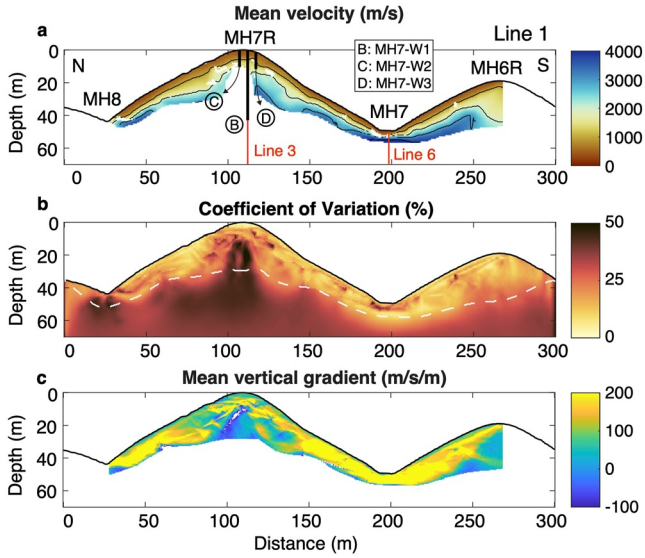

Figure 4. Results of Line 1 inversion using THB rj-MCMC (Huang et al., 2021). (a) Mean velocity model with contour lines at 1,000, 2,000, 3,000, and 4,000 m/s. The model is masked out where no geophones are present (edges of survey), below the deepest raypath, and where the coefficient of variation (CoV; standard deviation/mean velocity) >30%. Vertical dashed lines highlight the locations of boreholes within 10 m of the survey line. From north to south, these include boreholes MH7-W2, MH7-W1, and MH7-W3 for Line 1. The orange vertical line indicates the intersection point of Lines 1 and 3. (b) Percent CoV with the deepest raypath as the white dashed line. (c) Mean vertical velocity gradient (m/s/m), masked out where there are no geophones and below the deepest raypath.

(Figure 4a). A second survey line (Line 2 in Figure 1b) was conducted parallel to bedding across MH7R with twice as many geophones in efforts to obtain deeper ray paths and resolve velocity below the ridge (see Figure S1 in Supporting Information S1). Line 2 resolves deeper material below the hillslopes, reaching Vp > 3,500 m/s above the elevation of the channel, but we were still unable to resolve the structure below 14 m at the ridgetop, likely indicating a near constant seismic velocity below this depth.

4.1.2. MH7 Channel (Line 6)

Much of the shallow velocity profile for Line 6 has low raypath density due to a high velocity contrast at shallower depth, which does not allow for deep raypaths without a longer source-receiver distance. Since weathering transitions happen at shallow (<5 m) depth below the channel, we show an interpolated version of the mean velocity (Figure 5a). Vp rapidly reaches 3,000 m/s within 1–5 m of the surface, with a slightly shallower high gradient zone farther east. The seismic survey configuration does not have sensitivity below ~10 m depth. Velocity for Line 6 agrees with Line 1 at their intersection (red line at 90 m). The MH2 channel (Lines 10–11) is shown in Figure S6 in Supporting Information S1 and reaches high velocities within 6 m of the surface on the western side, and within 2 m further east.

4.1.3. MH3R and MH2R Bedding-Parallel (Line 7)

Line 7 is the same transect shown in Huang et al. (2021). Four boreholes at MH3R are within 10 m of Line 7: MH3-W1, MH3-W2, MH3-W3, and MH3-W4. Results of this survey indicated an upslope-thickening weathering profile for MH3R, with low-velocity (<1,000 m/s) material extending 5 m below the ridge and <1 m below the MH3 channel (Figure 6a). Three boreholes at MH2R are within 10 m of Line 7: MH3-W5, MH3-W6, and MH3-W7. The MH2R ridgetop presents a different velocity structure than its neighbor. Low-velocity material extends to a similar depth of 5–6 m, but mid-velocity material extends further below the ridgetop than at MH3R. Velocities at MH2R increase gradually, remaining at 2,000 m/s even at depths of 20 m below the ridge. The 3,000 m/s contour is barely reached within the resolvable depth range.

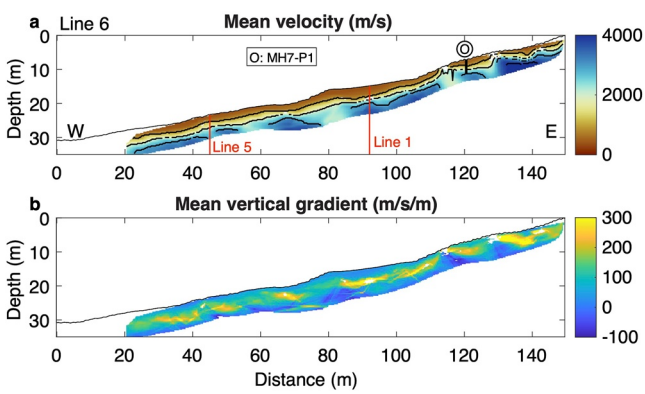

Figure 5. Results of Line 6 inversion. (a) Interpolated mean velocity model with contour lines at 1,000, 2,000, 3,000, and 4,000 m/s. The model is masked out below the deepest raypath and where CoV >40%. Black dashed lines highlight the locations of boreholes within 10 m of the survey line. Red lines indicate the intersection points with Line 5 (45 m) and Line 1 (90 m). (b) Mean vertical velocity gradient (m/s/m).

4.1.4. MH3R Perpendicular (Line 8)

Three boreholes at MH3R are within 10 m of Line 8: MH3-W1, MH3-W3, and MH3-W4. The velocity contours are surface-parallel for most of the west-facing slope, though the 3,000 m/s contour is more variable (Figure 7a). The east-facing slope has a highly variable thickness of weathered material, with Vp > 2,000 m/s reached at the surface near the ridgetop, and at > 25 m depth toward the east channel. The shallow high-velocities east of the ridge correspond to the location of the east-dipping sandstone cap that tops each ridge. While the structures of the east- and west-facing slopes are different, there is not a consistent difference in weathered zone thickness (Figure S12 in Supporting Information S1). Bedding-perpendicular Line 9 also reveals subtle variations in velocity structure that may relate to lithologic contrasts (Figure S5 in Supporting Information S1), but the overall east- and west-facing structures do not appear to differ dramatically. All bedding-perpendicular lines indicate largely surface-parallel weathered material that thins at the channel and thickens at the ridge.

4.2. Borehole and Seismic Velocity Comparison

We do not attempt to analyze the soil-saprolite boundary (Interface 1 at 0.3–0.5 m, Pedrazas et al., 2021) using seismic refraction, as the relatively

21699011, 2023, 7, Downloaded from https://agupubs.onlinelibrary.wiley.com/doi/10.1029/2023JF007254 by Test, Wiley Online Library on [03/07/2023]. See the Terms and Conditions (https://onlinelibrary.wiley.com/terms-and-conditions) on Wiley Online Library for rules of use; OA articles are governed by the applicable Creative Commons License

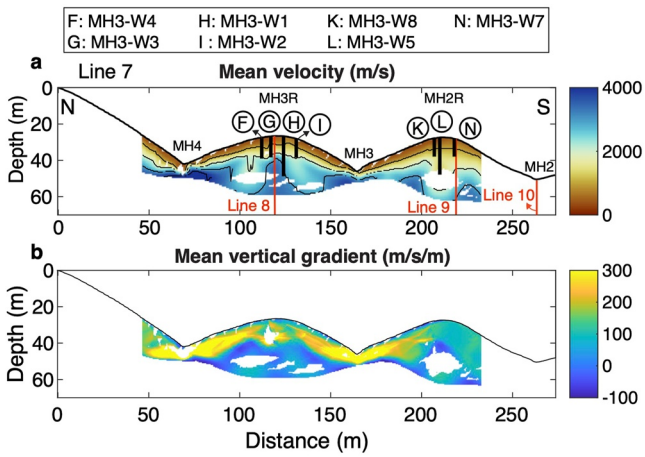

Figure 6. Results of Line 7 inversion. (a) Mean velocity model with contour lines at 1,000, 2,000, 3,000, and 4,000 m/s. The model is masked out below the deepest raypath and where CoV >30%. Black dashed lines highlight the locations of boreholes within 10 m of the survey line. From north to south, these include boreholes MH3-W3, MH3-W4, MH3-W1, and MH3-W2 on MH3R, and MH3-W6, MH3-W5, and MH3-W7 on MH2R. The orange vertical lines indicate the intersection points of Line 7 with Lines 8 (MH3R) and Line 9 (MH2R). (b) Mean vertical gradient (m/s/m). Note the gradient color scale ranges from −100 to 300 m/s/m.

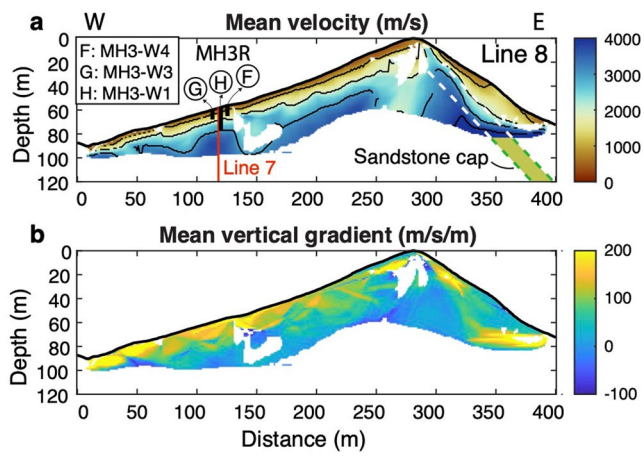

Figure 7. Results of Line 8 inversion using THB rj-MCMC. (a) Mean velocity model with contour lines at 1,000, 2,000, 3,000, and 4,000 m/s. The model is masked out below the deepest raypath and where CoV >30%. Black dashed lines highlight the locations of boreholes within 10 m of the survey line. From west to east, this includes boreholes MH3-W4, MH3-W1, and MH3-W3. The orange vertical line indicates the intersection point with Line 7. The white and green dashed lines and SS represent the sandstone capstone. (b) Mean vertical gradient (m/s/m).

low seismic source frequency from hammer shots (typically 20–30 Hz) and p-wave picking uncertainty do not allow us to capture submeter structure. Using seismic refraction data, we can delineate deeper interfaces using a velocity contour or the peak vertical velocity gradient. Here, we present the results of both. Material above the Interface 2 depth (pervasively fractured saprolite) gradually increases in Vp from 400 to 1,000 m/s. The average Vp across the borehole-defined Interface 2 depth range for all ridges is 1,284 ± 203 m/s (Figure 8). For each ridge, the Interface 2 Vp varies with the orientation of the seismic line relative to bedrock bedding, with bedding-perpendicular lines often the fastest. Uncertainty in the Interface 2 depth from borehole data also adds to the velocity range. Material below the Interface 2 depth (weathered bedrock) is generally 1,300–2,000 m/s. Average velocity corresponding to the Interface 3 depth is 1,973 ± 435 m/s across all lines. Vp at Interface 3 differs significantly between the three ridges (Figure 8). Interpretation of Interface 3 from the borehole is based primarily on a decrease in yellowness hue with depth (inferred as a decrease of chemical weathering) and a decrease in fracture density (Pedrazas et al., 2021). However, the different Vp ranges for Interface 3 between ridges suggest that these borehole changes may not map onto a specific velocity contour.

The maximum vertical velocity gradient captures the fastest increase of Vp with depth, which may be comparable to borehole interfaces. However, vertical velocity gradient does not exhibits a clear peak that can be easily traced across a hillslope. Rather, a zone of high gradient is observed in all profiles (Figures 4c, 5b, and 7b). At the MH7R ridgetop, we see a zone of high velocity gradient from around 3 m to 7–10 m depth (Figure 9b). At MH3R, this high gradient zone appears as 2 peaks centered at 3 and 10 m. For MH2R, the high gradient zone is gradual without a clear peak, stretching from 2 to 12 m. There is not a clear relationship between velocity gradient and borehole property gradients (colored boxes in Figure 9b), but the most rapid changes in borehole properties do occur within the highest velocity gradient zone (~3–13 m) for each survey. Borehole transitions such as the increase in blowcount rate occur more gradually for MH2R (Pedrazas et al., 2021), consistent with its much lower velocity gradient.

Orientation of the seismic lines also influences the gradient structure. Across all three ridges, bedding-parallel lines have more pronounced peak gradient features, and bedding-perpendicular lines show a more consistent lower gradient, reflective of a more gradual increase in velocity (see Figures 4c and 6b vs. Figure 7b). It is difficult to distinguish Interfaces 2 and 3 using the velocity gradient. Rather, a relatively high-gradient zone, across which borehole properties change most dramatically, spans both interfaces.

4.3. Hillslope Analysis

To examine aspect-dependency in the subsurface, we compare the depth to the saprolite-weathered bedrock transition (Interface 2, 1,284 ± 203 m/s) and weathered-fractured bedrock transition (Interface 3, 1,973 ± 435 m/s) on sets of north-facing and south-facing hillslopes that share the same ridge or the same catchment. Figure 10 shows the depth to Interface 2 with distance from the ridge along a straight-line transect. For all hillslopes, the saprolite layer thickens toward the ridge, and the depth to the base of the saprolite appears nearly identical on north- and south-facing slopes, though it is variable from channel to ridge (Figures 10a and 10c).

Averaged depths to the 700 m/s, 1,284 m/s (Interface 2 contour), 1,973 m/s (Interface 3 contour), 2,500 m/s, and 3,000 m/s velocity contours present an inconsistent relationship between aspect and velocity, with the average south-facing depth sometimes shallower and sometimes identical to

21699011, 2023, 7, Downloaded from https://agupubs.onlinelibrary.wiley.com/doi/10.1029/2023JF007254 by Test, Wiley Online Library on [03/07/2023]. See the Terms and Conditions (https://onlinelibrary.wiley.com/terms-and-conditions) on Wiley Online Library for rules of use; OA articles are governed by the applicable Creative Commons License

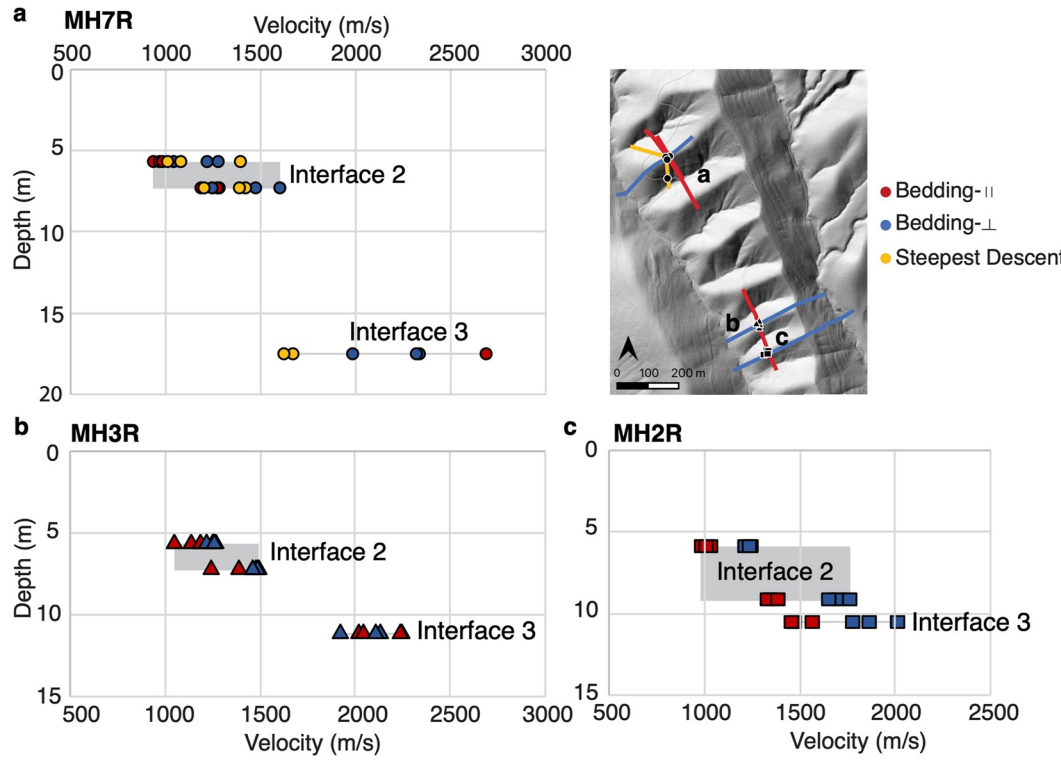

Figure 8. Seismic velocity at borehole interfaces 2 and 3 identified by Pedrazas et al. (2021) for (a) MH7R, (b) MH3R, and (c) MH2R. An upper and lower depth bound is plotted for Interface 2 based on the depth standard deviation from Pedrazas et al. (2021). Marker colors indicate the survey line orientation.

north-facing slopes. When the Interface 2 depth is normalized with distance from the ridge (Figure S8 in Supporting Information S1), the MH7 south-facing slope does appear to have a shallower Interface 2 depth than the MH7 or MH8 north-facing slopes. However, at MH2, the normalized south-facing slope has a greater Interface 2 depth. Normalized average depth to velocity contours similarly shows shallower weathering depth on the MH7 south-facing slope but deeper or identical weathering depth on the MH2 south-facing slope (Figure 10). Through the combined analysis of borehole data and geophysics, we find no consistent difference in saprolite thickness with slope aspect for our surveyed ridges. This appears to be true for slopes within the same catchment (i.e., MH7 S and MH7 N), and for slopes sharing the same ridge (i.e., MH7 S and MH8 N).

We also compared Interface 2 depth between the MH8 north-facing and MH7 south-facing slopes along the steepest descent survey orientation (Lines 4 and 5; Figure S7 in Supporting Information S1. The steepest-descent profiles also do not demonstrate clear differences in Interface 3 depth between north-facing and south-facing slopes, although the Interface 3 depth does appear shallower below the MH7 south-facing slope in the mid-slope position (Figure S9c and S9d in Supporting Information S1).

4.4. Trade-Off Between Porosity and Saturation

4.4.1. 1D Porosity and Saturation at MH7

Following Section 3.3, our rock physics model indicates a tradeoff between relative saturation and porosity that can predict the same seismic velocity measured at depth. We varied the mineral composition between quartz, feldspar and chlorite, but we did not consider clay at the top few meters depth in the porosity modeling and may have overestimated porosity near the soil-saprolite transition zone if there is presence of higher clay mineral content. However, the relative amount of each mineral component does not have a large influence on porosity (Figure 11a; Callahan et al., 2020). Therefore, while we have not included all possible mineral components (i.e., there is >1wt% organic carbon noted in Pedrazas et al., 2021), mineral composition is likely only a small source of error in the porosity estimate. Similarly, we do not take into account the capillary forces in the unconsolidated zone at shallower depth, which may impact the modeled porosity near-surface (Solazzi et al., 2021).

21699011, 2023, 7, Downloaded from https://agupubs.onlinelibrary.wiley.com/doi/10.1029/2023JF007254 by Test, Wiley Online Library on [03/07/2023]. See the Terms and Conditions (https://onlinelibrary.wiley.com/terms-and-conditions) on Wiley Online Library for rules of use; OA articles are governed by the applicable Creative Commons License

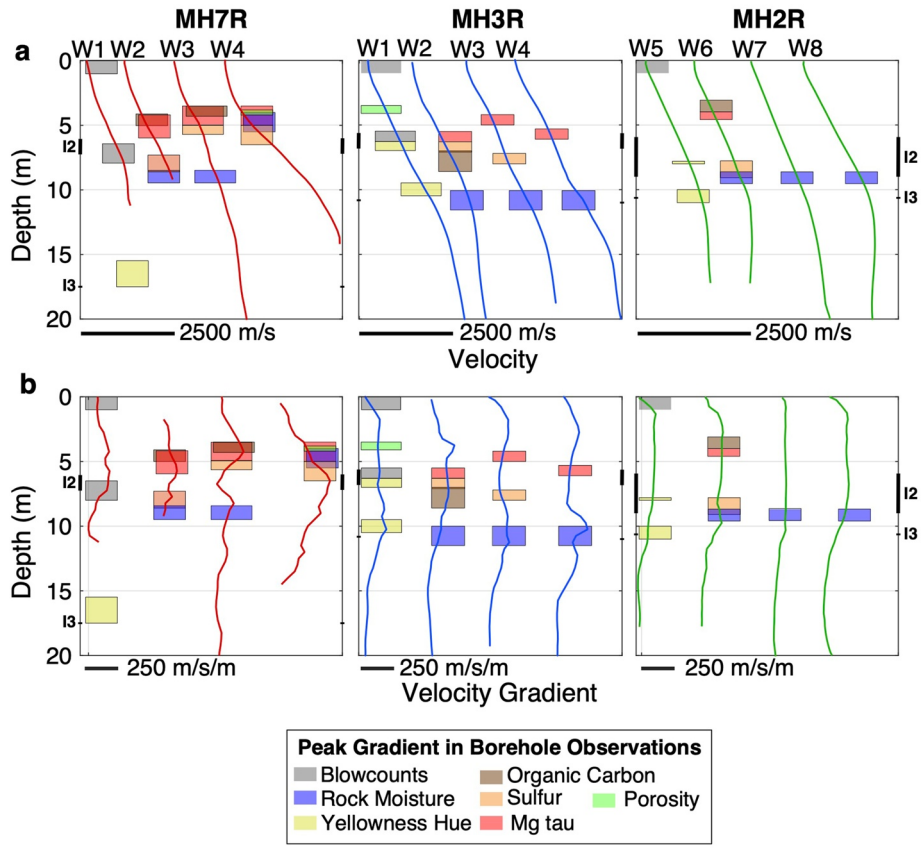

Figure 9. Velocity (a) and velocity gradient (b) profiles for each borehole across the three ridges. Each 1D profile represents the velocity and velocity gradient at each borehole averaged across all seismic line orientations. Colored boxes represent depth ranges where the vertical gradient of each borehole property is highest. Interface 2 (I2) and Interface 3 (I3) depths are shown on the edge of each plot (from Pedrazas et al., 2021). Only the deep boreholes MH7-W1, MH3-W1, and MH2-W5 have observations of blowcount rate and yellowness hue. The absence of a data type for a given profile indicates there were no sharp changes in that property with depth. The *x*-axis is stretched to space out each borehole, and a scale bar is shown for velocity and velocity gradient.

The rock physics model applied at 1 and 6 m depth (Figure 11a) indicates that, below ~40%, changes in saturation do not affect the modeled total porosity (Φ_{total}). On the other hand, small increases in saturation >40% necessitate dramatic increases in porosity to explain the same velocity observation. Since precise measurements of saturation along depth are absent and shallow depths are unlikely to have saturation greater than

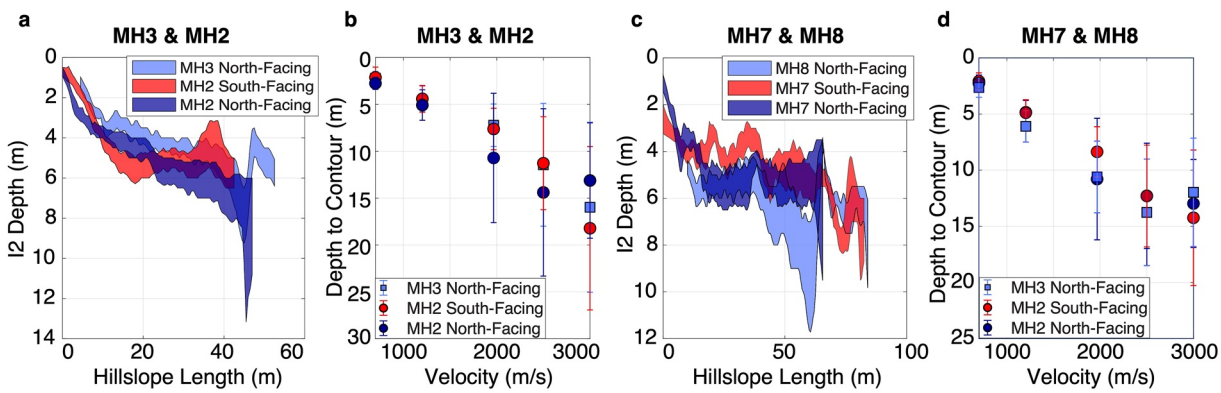

Figure 10. Comparison of weathering thickness on north- versus south-facing hillslopes for Line 6 (a, b), and Line 1 (c, d). Depth to Interface 2 (I2; saprolite-weathered bedrock) with hillslope length (a, c) is shown based on the I2 velocity range (1,284 ± 203 m/s velocity contours). Average depths to various velocity contours are shown in (b, d), including the average Interface 2 velocity contour (1,284 m/s) and average Interface 3 velocity contour (1,973 m/s).

21699011, 2023, 7, Downloaded from https://agupubs.onlinelibrary.wiley.com/doi/10.1029/2023JF007254 by Test, Wiley Online Library on [03/07/2023]. See the Terms and Conditions (https://onlinelibrary.wiley.com/terms-and-conditions) on Wiley Online Library for rules of use; OA articles are governed by the applicable Creative Commons License

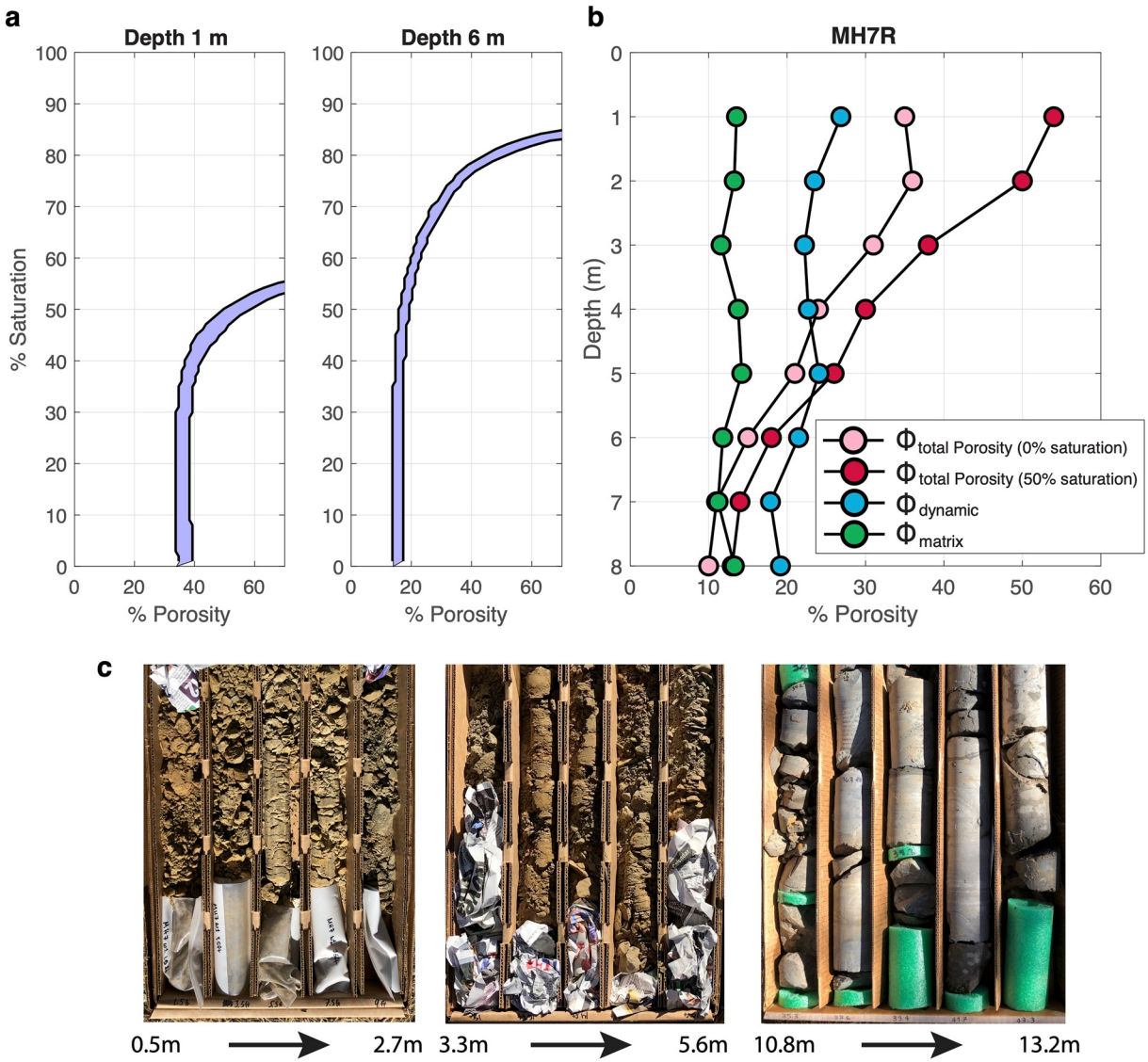

Figure 11. 1D rock physics model at MH7R (Line 1, a). (a) Tradeoff between saturation and porosity at MH7R at different depths based on the rock physics model using seismic refraction. Each point along the curve represents a porosity/saturation value that predicts a nearly identical (<1% difference) Vp at that depth. The width of the purple-shaded area represents the variation within the assumed mineral composition (i.e., 20% quartz, 30% feldspar, 50% chlorite, vs. 30% quartz, 50% feldspar, 20% chlorite, etc.). (b) Porosity with depth from the rock physics model (Φ_{total}) based on the average velocity profile across all wells at MH7R. Measured matrix porosity (Φ_{matrix}) from cores at MH7-W1, MH7-W2, and MH7-W3 interpolated to a 1 m depth is shown in green. The dynamic porosity ($\Phi_{dynamic}$) is based on neutron probe measurements at MH7-W2 and MH7-W3, with outliers removed and also interpolated to 1 m depth. (c) Core photos along different depths that show change of fracture density from shallow to greater depth. Note that samples shallower than 6 m depth are highly fractured and chemically weathered.

40% in August (5 months into the dry season) when our seismic survey was performed, we assume relative saturation is 0% for the whole depth profile. Although 0% saturation is also incorrect, the porosity estimate is insensitive to saturation values when saturation is less than 40% (Figure 11a).

Matrix porosity (Φ_{matrix} in Figure 11b) measured from core samples is consistently <15% for MH7. Matrix porosity does not account for fractures, which we know to be pervasive in the upper 6 m (Pedrazas et al., 2021). The dynamic porosity ($\Phi_{dynamic}$ in Figure 11b; see Equation 2) ranges from >25% at a 1 m depth to ~17% at a 7 m depth. If we assume the matrix is perennially saturated, $\Phi_{dynamic}$ represents a lower bound for the total porosity. Finally, the modeled total porosity (Φ_{total}) ranges from 35% at a 1 m depth to 9% at an 8 m depth, assuming 0% saturation (Figure 11b).

21699011, 2023, 7, Downloaded from https://agupubs.onlinelibrary.wiley.com/doi/10.1029/2023JF007254 by Test, Wiley Online Library on [03/07/2023]. See the Terms and Conditions (https://onlinelibrary.wiley.com/terms-and-conditions) on Wiley Online Library for rules of use; OA articles are governed by the applicable Creative Commons License

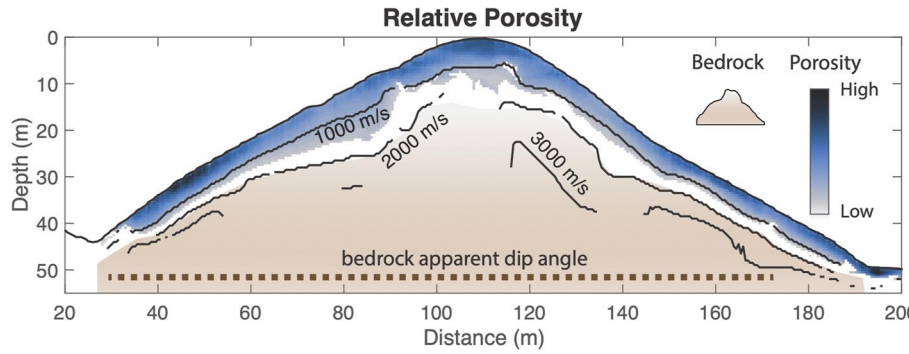

Figure 12. 2D relative total porosity model of the MH7R hill (based on seismic line 1). Light to dark blue colors represent an increase of porosity. The light brown color represents bedrock location, and the dashed line indicates the apparent dip of the bedrock. The contour lines are the seismic P-wave velocity (Vp). The rock physics model was applied to the 2D velocity model, with velocity >1,500 m/s masked out.

Total porosity (Φ_{total}) rapidly decreases between 2–3 m and 5–6 m depth, and then stabilizes below 6m. At ~5–6 m depth, the modeled Φ_{total} is less than $\Phi_{dynamic}$. This depth corresponds with the Interface 2 (saprolite-weathered bedrock) boundary, where the core changes from pervasively to discreetly fractured (Figure 11c). Total porosity for MH3R and MH2R are shown in Figures S10 and S11 in Supporting Information S1, respectively, and similarly show Φ_{total} ranging from 30% to 35% at the surface to 10% by 8 m depth. MH2R has higher Φ_{total} in the upper 6 m than MH3R, and a more gradual change in porosity with depth, consistent with the deeper low-velocity material observed at MH2R in Figure 6.

4.4.2. 2D Porosity at MH7

The rock physics model can also be applied on a 2D scale to examine the landscape porosity distribution across the north and south facing hillslopes. 2D models show that the most pronounced decrease in porosity occurs within the saprolite layer (<6 m depth, Figure 12). Below this depth, porosity is low and only decreases gradually. The mean porosity models represent the average of porosity estimated using varied percentages of feldspar, quartz, and chlorite (see Section 3.3). To construct a 2D model of bulk porosity, we assumed saturation was 0% (see Section 4.4.1). Assuming a different 2D saturation model would change the results of our model, particularly at shallow depths (Figure 11b). However, when saturation is low (<40% and 50% at 1 and 6 m depth, respectively), variation in the saturation model does not have a dramatic effect on modeled porosity (Figure 11a). The 2D model reveals there is heterogeneity in total porosity across each hillslope.

5. Discussion

5.1. Borehole and Seismic Velocity Comparison

Seismic refraction is a useful tool to determine broad scale subsurface structure by identifying transitions in P-wave velocity (Vp) that can correspond to rock properties associated with weathering. However, seismic refraction is not expected to perfectly capture borehole-inferred properties since it is sensitive to larger spatial scales (meter-scale; Flinchum et al., 2022), whereas the borehole diameter is 6.35–12.7 cm and has cm-level sampling resolution for some measurements (Pedrazas et al., 2021). Vp is a measurement of bulk material strength that depends on lithology, porosity, moisture content, and chemical weathering. Several studies have shown good agreement between Vp and rock strength or fracture density (e.g., Clarke & Burbank, 2011; Flinchum, Holbrook, Rempe, et al., 2018; Holbrook et al., 2019; Lee and de Freitas, 1990; West et al., 2019), as well as chemical mass loss (Gu et al., 2020).

Seismic refraction surveys at Rancho Venada capture a critical zone structure that closely matches the borehole-derived structure presented by Pedrazas et al. (2021). Material with Vp < 1,284 m/s is interpreted as saprolite, consistent with other studies that find saprolite Vp < 2,000 m/s (Befus et al., 2011) or < 1,200 m/s (Flinchum, Holbrook, Rempe, et al., 2018; Leone et al., 2020). The core within this zone is "pervasively fractured," oxidized, and mechanically weak (Pedrazas et al., 2021). An increase in vertical velocity gradient occurs toward the bottom of the saprolite layer, marking a gradual transition to weathered bedrock. From the 1,284 m/s

21699011, 2023, 7, Downloaded from https://agupubs.onlinelibrary.wiley.com/doi/10.1029/2023JF007254 by Test, Wiley Online Library on [03/07/2023]. See the Terms and Conditions (https://onlinelibrary.wiley.com/terms-and-conditions) on Wiley Online Library for rules of use; OA articles are governed by the applicable Creative Commons License

21699011, 2023, 7, Downloaded from https://agupubs.onlinelibrary.wiley.com/doi/10.1029/2023JF007254 by Test, Wiley Online Library on [03/07/2023]. See the Terms and Conditions (https://onlinelibrary.wiley.com/terms-and-conditions) on Wiley Online Library for rules of use; OA articles are governed by the applicable Creative Commons License

contour, and the onset of the high gradient zone, we can determine the thickness of the saprolite across the landscape as 0–2 m thick at the channels, then increasing in thickness with lateral distance from the channel. It remains ~4–6 m thick under most of the hillslope and thickens only slightly approaching the ridgetop (Figures 10a and 10c). Saprolite thickness is nearly identical between ridges, despite a 25m difference in relief from MH7R to MH3R and MH2R.

Below the saprolite layer, Vp increases from ~1,200 to 2,000 m/s generally in less than 10 m. This Vp range is variably thick across the landscape and is inferred to be weathered bedrock based on the presence of open, oxidized fractures (Pedrazas et al., 2021). Below this, the core exhibits a sudden decrease in yellowness hue and decrease in fracture density from "discreetly" to "rarely" fractured (Figures 2 and 9; Pedrazas et al., 2021). The bottom of the weathered bedrock is also upslope-thickening (Figure S9 in Supporting Information S1).

Velocity below the weathered bedrock increases gradually from 2000 to >3,000 m/s. The core in this depth range is rarely fractured, and fractures present are closed and unoxidized (Pedrazas et al., 2021). The gradual increase in Vp may be due to further reductions in fracture density with depth and an increase of overburden. When porosity is low, even a <5% decrease in crack volume can increase Vp by 1,000 m/s in granites (Flinchum et al., 2022). Unweathered, unfractured bedrock is more likely to be reached at ~20 m depth where velocities reach 3,000 m/s and velocity gradient approaches zero. Several studies use 4,000 m/s as the bedrock velocity contour (Befus et al., 2011; Gu et al., 2020; Holbrook et al., 2014); however, 3,000 m/s is still within the expected range for unweathered sedimentary bedrock with 10% porosity (Dvorkin et al., 2021; Eberhart-Phillips et al., 1989; Mavko et al., 2009). A collection of Vp measurements from laboratory and field settings shows that clay-rich rocks commonly have a fresh bedrock velocity between 2000 and 4,000 m/s (Lee, 2018). Velocity from the channel surveys, which should be relatively fresh, are mostly <4,000 m/s (Figure 5; Figure S6 in Supporting Information S1). All of our surveys therefore reach unweathered, rarely fractured bedrock at or above the channel elevation, and we do not see the topography of the weathering front that systematically mirrors surface topography as expected for a highly stressed tectonic environment (Moon et al., 2017).

The transition from saprolite to weathered bedrock (Interface 2), from weathered to fractured bedrock (Interface 3), and from fractured to unfractured bedrock are difficult to distinguish as separate interfaces using velocity contours or the vertical velocity gradient. In particular, the seismic velocity at interface 3 ranged between 1,600 m/s and 2,700 m/s for MH7R, 1,900 m/s and 2,300 m/s for MH3R, and 1,400 m/s and 2,000 m/s for MH2R, which are not consistent across different ridges (Figure 8). As a result, using absolute seismic velocity to identify interface 3 may not be reliable. While this may be due in part to variability in velocity structure between different survey line orientations, the lack of a clear distinction between interfaces is also visible in the borehole data. For example, the depth of dynamic rock moisture storage from neutron probe counts at 8–9 m below ridgetops generally exceeds the Interface 2 depth (6 m) but not the Interface 3 depth (11–17 m). While we interpret a "layered" critical zone structure, our observations suggest a broad, gradual zone of physical and chemical weathering, starting a few meters below the surface, and extending to ~20 m below the ridgetops (Figure 11). This gradual zone of increasing material strength is similar to critical zone models presented at Shale Hills (West et al., 2019) and Calhoun Observatory (Holbrook et al., 2019).

From the analysis of borehole data, seismic velocity, and vertical velocity gradient, we can characterize critical zone structure at Rancho Venada as including (a) a thin (<1 m) soil layer (Pedrazas et al., 2021), (b) a ~5 m thick saprolite layer that thins abruptly at the channels, across which most chemical reactions occur and mechanical strength dramatically changes, (c) a weathered bedrock layer of high velocity gradient in which the presence of open, oxidized fractures gradually decreases, and (d) a variably thick-fractured bedrock layer with closed, unoxidized fractures.

5.2. Characterizing Weathering Across Hillslopes

Our seismic refraction surveys capture changes in the material properties of the subsurface that align with borehole observations, allowing us to project Interfaces 2 and 3 across the landscape. With these interfaces estimated at the landscape scale, we can explore how the weathering structure varies with respect to slope aspect and bedding orientation and exploit relationships between P-wave velocity (Vp) and rock properties to model subsurface bulk porosity.

5.2.1. North Versus South Facing Hillslopes

Several seismic refraction studies have observed thicker saprolite and weathered rock on north-facing slopes and a thinner weathered layer on south-facing slopes (Befus et al., 2011; McGuire et al., 2014; Nielsen et al., 2021;

21699011, 2023, 7, Downloaded from https://agupubs.onlinelibrary.wiley.com/doi/10.1029/2023JF007254 by Test, Wiley Online Library on [03/07/2023]. See the Terms and Conditions (https://onlinelibrary.wiley.com/terms-and-conditions) on Wiley Online Library for rules of use; OA articles are governed by the applicable Creative Commons License

Wang et al., 2021). However, most of these sites have a different lithology and climate regime than Rancho Venada, both of which are shown to affect the magnitude of weathering asymmetry with aspect (Inbar et al., 2018; Pelletier et al., 2018) and the thickness of weathered material (Hahm, Rempe, et al., 2019).

The stark difference in vegetation (Figure 1) and the thicker soil profiles on north- versus south-facing hillslopes indicate that aspect-dependent solar radiation does play a role in surface landscape processes at Rancho Venada (Pedrazas et al., 2021). Tree roots here can extend 14 m laterally and 6–8 m down into the weathered bedrock (Hahm et al., 2022), and therefore we may reasonably expect roots to contribute to bedrock weathering through biochemical or biomechanical processes (i.e., Pawlik et al., 2016). However, seismic refraction does not show a clearly thicker saprolite layer on north-facing slopes (Figure 10), consistent with borehole observations from Pedrazas et al. (2021). This result is contrary to what we might expect in a precipitation-limited environment (as in Pelletier et al., 2018), where increased soil moisture and root-rock interactions on north-facing slopes can exert a top-down influence on critical zone structure.

Other studies have also observed a lack of clear aspect-dependent saprolite thickness at sites with clear aspect-dependent vegetation density. For example, a site named Blue Oak Ranch Reserve that is ∼200 km south of Rancho Venada and shares similar lithology and climate does not show a clear aspect-dependent saprolite thickness (Donaldson et al., 2023). In addition, the south-facing slopes of the Santa Catalina Mountains in Arizona have thicker saprolite, despite a lower tree density (Leone et al., 2020). This is attributed to the orientation of bedrock foliation planes, which dip into the surface topography at a high angle on the south-facing slope and are oriented parallel to the north-facing slope. The high angle intersection on the south-facing slope facilitates enhanced weathering along the weak foliation planes, creating thicker saprolite. At Rancho Venada, bedding and dominant fracture planes are oriented N10°W; therefore, the apparent dip of the lithology and of the most abundant fracture set is nearly horizontal for the bedding-parallel seismic survey lines. There is no significant difference in the angle between bedding or fracture planes and the surface topography for north versus south-facing slopes. Therefore, increased hydraulic conductivity along planes of weakness (e.g., bedding planes) cannot explain the lack of north/south aspect-dependency below the soil layer at Rancho Venada.

It is possible that the top-down influence of tree roots on the critical zone does not extend deep enough or is masked out by more dominant landscape processes that create symmetrical hillslopes. Regional tectonic stress, hydrologic properties of the bedrock, or the influence of bedding orientation on the landscape could contribute to saprolite thickness at Rancho Venada. In this case, top-down climate processes may be negligible below the soil layer. Still, given the stark contrast in vegetation density with aspect, the documented seasonal use of bedrock moisture by tree roots at depths >5 m at this site (Hahm et al., 2022), and the potential for tree roots to expand fractures and promote chemical weathering within fractured rock (Hasenmueller et al., 2017), it is worth considering the role of climate and root distribution in influencing weathering depth.

A plausible explanation for the similar weathering thickness on north- and south-facing slopes is that weathering processes at RV have not always been precipitation-limited. Oxygen isotope analysis of sediment cores from Clear Lake (∼20 km from Rancho Venada) reveals that from 13ka–80ka the climate of the region was 8°C colder with ∼1,000 mm/yr more precipitation than its present condition (Adam & West, 1983). This cooler, wetter climate regime may have resulted in minimal differences in tree density with aspect or a different tree species composition altogether (Adam & West, 1983; Cole, 1983). Assuming a steady-state landscape with a 0.1 mm/yr erosion rate (Pedrazas et al., 2021), a 6 m thick saprolite would have a residence time of 60 ky, and therefore most of the saprolite at Rancho Venada would have been influenced by a cooler climate regime in the past. A shift from cold-wet to warm-dry climate conditions in the last 13 ka may therefore only impact the soil layer and the shallowest part of the saprolite. This may explain why the vegetation density and soil thickness are different between north- and south-facing slopes, while the saprolite thickness is roughly the same.

The influence of past climate on slope aspect asymmetry has been documented across many regions. At Shale Hills in Pennsylvania, frost-cracking during the last glacial maximum interacted with microtopography to drive the hillslope asymmetry observed today, despite a lack of frost-cracking conditions in the present climate (Wang et al., 2021; West et al., 2019). Likewise, the strong slope asymmetry currently observed in the Redondo Mountains in New Mexico can be explained by vegetation regimes present in the cooler Pleistocene (Istanbulluoglu et al., 2008). Past climate can also play a significant role in aspect-dependent surface topographic gradients and drainage densities (McGuire et al., 2014).

21699011, 2023, 7, Downloaded from https://agupubs.onlinelibrary.wiley.com/doi/10.1029/2023JF007254 by Test, Wiley Online Library on [03/07/2023]. See the Terms and Conditions (https://onlinelibrary.wiley.com/terms-and-conditions) on Wiley Online Library for rules of use; OA articles are governed by the applicable Creative Commons License

5.2.2. Porosity

Characterizing water storage at the landscape scale is crucial in Mediterranean climate environments. Water stored below the soil during wet seasons can be accessed by vegetation during the growing season in dry summers, and help sustain them through drought (Hahm et al., 2022). Several recent studies have applied rock physics models to estimate total porosity from seismic refraction data (e.g., Holbrook et al., 2014; Pasquet et al., 2016; Flinchum, Holbrook, Rempe, et al., 2018; Flinchum, Holbrook, Grana, et al., 2018; Hayes et al., 2019; Gu et al., 2020; Callahan et al., 2020). The parameters known to influence Vp include elastic moduli of the mineral composition, porosity, and saturation level. Saturation with depth can be measured from drying and weighing material (Holbrook et al., 2014), Vp/Vs ratio from downhole geophysics such as from sonic velocity logs (Gu et al., 2020), or nuclear magnetic resonance surveys (Flinchum, Holbrook, Grana, et al., 2018; Holbrook et al., 2019). Without direct measurements of saturation, the rock physics model explores a nonlinear relationship between porosity and saturation (Figure 11a).

Despite not having direct measurements of absolute saturation with depth, we are able to take advantage of multiple datasets to explore porosity at the landscape scale. The matrix porosity (Φ_{matrix}), measured from chips of the core, is assumed to be perennially saturated porosity that changes little with depth at our study hills. Incorporating $\Delta\theta$ from neutron probe surveys suggests that additional storage must be available to accommodate the observed seasonally dynamic water content. The dynamic porosity ($\Phi_{dynamic}$) therefore represents a lower bound estimate of the total porosity. Modeling bulk porosity from seismic refraction allows us to estimate a total porosity that reflects the unsaturated, pervasively fractured nature of the core. Our total porosity distribution ranges from 35% at the surface to ~9% at an 8 m depth (Figure 11b), implying a significant volume of fracture porosity.

While there are significant sources of uncertainty (e.g., mineral composition, empirical parameters, saturation) in the rock physics model such that our estimates of bulk porosity are not exact, the relative decrease in bulk porosity across the saprolite-weathered bedrock boundary matches high fracture density in core photos (Figure 11c) and material strength from the core that is not represented by matrix porosity alone. Additionally, the extensive hydrologic datasets at this site provide a check on our rock physics model, as total porosity must be higher than the observed water storage (Hahm et al., 2022). The agreement between seismically determined porosity gradients and transitions in fracture density and moisture content from boreholes implies that our seismic surveys can be deployed at a larger scale to capture porosity transitions where boreholes are absent. A combination of other geophysical datasets, such as incorporating electrical resistivity measurements, could provide a better constraint on the lateral distribution of saturation (e.g., Blazevic et al., 2020; Chen & Niu, 2022).

5.3. Broader Implications to Critical Zone Models

Weathering structure at Rancho Venada can inform mechanistic features of critical zone development in semi-arid landscapes. Upslope thickening topography of the weathered layers suggests that the hydraulic conductivity model proposed by Rempe and Dietrich (2014), in which the drainage of chemically equilibrated groundwater controls the fresh bedrock boundary, could apply to this landscape. This model predicts a permanent water table limiting the extent of chemical weathering reactions, but we find no evidence of a permanent water table here within the depth range of the weathered zone (Hahm et al., 2022; Pedrazas et al., 2021). Water was observed in the boreholes 30–35 m below the surface for MH7R, and 15–21 m below the surface for MH3R and MH2R (Hahm et al., 2022; Pedrazas et al., 2021). However, the present-day water table may not align with the interface depths if the water table has dropped since the cooler and wetter climate of the Pleistocene. Alternatively, the nested reaction fronts proposed by Lebedeva and Brantley (2013) and Brantley et al. (2017) could describe Rancho Venada's weathering structure. Lebedeva and Brantley (2020) show that in settings with low infiltration rate, reaction fronts can be located above the water table.

Pedrazas et al. (2021) found a roughly linear scaling relationship between hillslope length and relief of interfaces 2 and 3. Both interfaces agree with the predicted elevation of fresh unweathered bedrock (Zb) defined by Rempe and Dietrich (2014). The elevation of the transition to unweathered bedrock (Interface 3) appears roughly linear from channel to ridge (Figure 13a). When normalized by the channel-ridgetop distance, the hillslope profiles sharing the larger ridgetop (MH8N and MH7S) have a steeper slope of interface 3 than profiles for the smaller ridges (MH6R, MH3R, MH2R), possibly indicating some variability in weathering processes between the lower versus higher relief ridges (Figure 13b). Our seismic profiles do not allow us to draw a strong conclusion on the

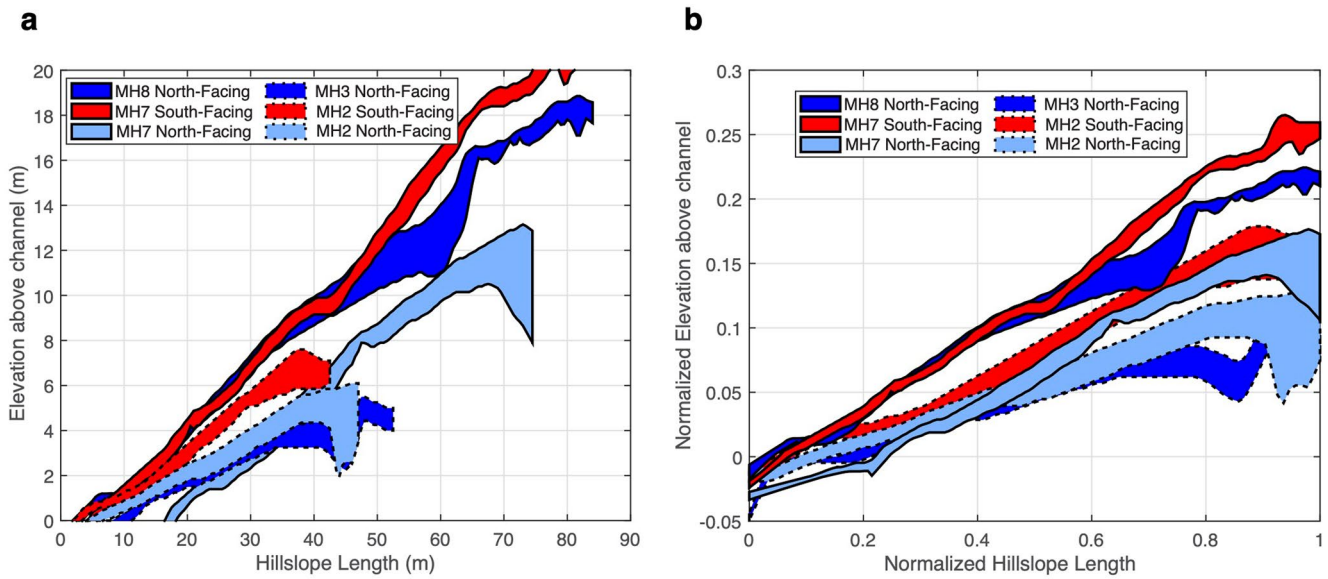

Figure 13. (a) Topography of interface 3 with hillslope length. The 6 different profiles are north (blue) and south (red) facing hills from seismic lines 1 and 7. Note 0 m in the *y*-axis represents the ground surface. (b) Same as a but the hillslope length of each profile is normalized. Note there is no consistent pattern between different profiles.

scaling relationship between hillslope length and relief, as proposed in Pedrazas et al. (2021). However, the agreement between seismic refraction and borehole data at this site means that additional seismic surveys spanning new ridges can be used to determine Zb depth even without boreholes present.

The ratio of gravitational and horizontal tectonic stresses can also determine the potential of subsurface fracturing and create deep weathering extending below the elevation of the channel in high-compressional regimes (St. Clair et al., 2015; Moon et al., 2017). Pelletier (2017) further suggests that soil production is highly influenced by topographic steepness that can open preexisting bedrock fractures. We performed seismic surveys both parallel and perpendicular to the least compressive stress orientation and did not observe low velocities below the channel elevation in either case. The lack of surface-mirroring weathering could be qualitatively used to assume low compressive stress parallel to the bedding strike at Rancho Venada. However, this site is less than 30 km away from the Bartlett Springs Fault system, and the principal compressive stress has been oriented roughly N-S (roughly parallel to the bedding strike) for at least the past 5 Myr (Atwater & Stock, 1998). With a contemporary maximum shear strain rate of ~50–100 nano-strain/yr (Xu et al., 2021; Zeng et al., 2018), we consider Rancho Venada subject to a high contemporary tectonic stressing rate relative to most regions of the U.S. Even though the current tectonic stressing rate is high, high internal strain rate and regional earthquake cycles may decrease material strength at Rancho Venada. This adds additional complexity to estimating fracture distribution from a simple stress model.

The sedimentary bedrock lithology has a distinct influence on the landscape at Rancho Venada, shaping the orientation and surface slope of the ridges and valleys (Pedrazas et al., 2021; Rich, 1971). The main study ridges are located within a turbidite sequence of interbedded mudstone and siltstone, with occasional meter-scale sandstone beds. The thicker weathered zone below MH2R is likely because MH2R intersects a larger proportion of fine-grained material (Pedrazas et al., 2021; Figure 6). East of our boreholes, the main north-striking ridge is capped by a thick (>5 m) sandstone bed. Line 8 features a high-velocity zone at shallow depth east of the ridgetop that matches the location of the MH3R sandstone cap (Figure 7), highlighting the role of sedimentary bedding in controlling weathering depth. The anti-dip hillslope just east of the ridge is dominated by mudstone (though the overall unit east of the main ridge has a higher sandstone component, as in Figure 1), and has much thicker low-velocity material (Figure 7). The difference in fracture or joint density between different major rock types (sandstone vs. mudstone) may influence the thickness of the critical zone here. Bedding orientation and changes in lithology may also help to explain why different orientations of seismic refraction survey lines result in different Vp values for the same location (Figure S3 in Supporting Information S1).

21699011, 2023, 7, Downloaded from https://agupubs.onlinelibrary.wiley.com/doi/10.1029/2023JF007254 by Test, Wiley Online Library on [03/07/2023]. See the Terms and Conditions (https://onlinelibrary.wiley.com/terms-and-conditions) on Wiley Online Library for rules of use; OA articles are governed by the applicable Creative Commons License

21699011, 2023, 7, Downloaded from https://agupubs.onlinelibrary.wiley.com/doi/10.1029/2023JF007254 by Test, Wiley Online Library on [03/07/2023]. See the Terms and Conditions (https://onlinelibrary.wiley.com/terms-and-conditions) on Wiley Online Library for rules of use; OA articles are governed by the applicable Creative Commons License

However, we do not find lithology or bedding structure to be as strong a control on critical zone structure at Rancho Venada as at some metamorphic sites (i.e., Leone et al., 2020). While there is thicker weathered material on the east-facing slope of Line 8, we do not observe a similar pattern for Line 9, which also runs perpendicular to bedding across an east- and west-facing slope (Figure S5 in Supporting Information S1). We therefore do not see a consistent contrast between east and west-facing slopes despite the vastly different intersection of bedding planes with surface topography (Figure 7). Future work to compare fracture orientation and surface slope with weathering depth, along with more detailed geologic mapping, may further flesh out the influence of the regional geology on the critical zone structure at this site.

6. Conclusions

We combine geophysics and borehole measurements to characterize lateral critical zone structure at Rancho Venada, a semi-arid sedimentary ridge-valley landscape in northern California, USA. Below the soil layer, seismic data reveal a weathered zone from 4 to 13 m below ridgetops, over which velocity increases from 1,000 to 2,500 m/s with a higher vertical velocity gradient. In combination with borehole data, we detect a transition from pervasively fractured and chemically weathered material to more competent material at a 5–6 m depth. This transition is interpreted as the saprolite-weathered bedrock transition, and is largely surface-parallel, with a slight thickening toward the ridges and sharp thinning at the channels. A second, deeper transition zone is observed in the borehole logs as yellowness hue further decreases. However, this transition zone cannot be detected by seismic refraction alone due to a lack of clear change of vertical velocity gradient. We interpret the deeper transition as the weathered to fractured bedrock boundary. Bedding-parallel and perpendicular seismic lines indicate that the critical zone thins toward the first and second order channels. We adopt a rock physics model based on the seismic velocity model to evaluate saprolite total porosity. The results suggest that inherited fractures from the bedrock contribute a substantial amount of pore space in the upper 6 m, and the lateral porosity structure varies strongly with hillslope position. Despite higher tree density and thicker soils on north-facing slopes, we observe an overall similar saprolite and weathered bedrock layer on both north- and south-facing slopes, contrary to what we might expect in a precipitation-limited environment. We suggest that the cooler, wetter climate experienced during the Pleistocene may have allowed for the presence of trees on both hillslopes, creating equally thick saprolite layers that have not yet adjusted to the current climate condition.

Data Availability Statement

Borehole data sets are published in Pedrazas et al. (2021). Volumetric water content and water table depths are published in Hahm et al. (2022). The THB rj-MCMC inversion is available on Zenodo (http://doi.org/10.5281/zenodo.4590999) and actively maintained in Github (https://github.com/MongHanHuang/THB_rjMCMC).

Acknowledgments
We thank the Brown and the Hemmi families for providing site access. Bill Dietrich, Associated Editor Jon Pelletier, and 3 anonymous reviewers provided insightful feedback that significantly improved the quality of this work. We are grateful for field assistance from Anna Weniger, Colleen Murphy, Jeng-Hann Chong, Kristen Fauria, and Maryn Sanders to carry out the seismic refraction surveys. We also thank Bill Dietrich, Kristen Fauria, and Alex Bryk for their insights and significant contributions in the earlier phase of the research. BHR is supported by the Carleton College Paglia post-baccalaureate fellowship. Part of this research is contributed by NSF-EAR-2012616 to MH.

References

Adam, D. P., & West, G. J. (1983). Temperature and precipitation estimates through the last glacial cycle from Clear Lake, California, Pollen Data. *Science*, *219*(4581), 168–170. https://doi.org/10.1126/science.219.4581.168

American Society for Testing and Materials (ASTM). (2022). Standard test method for standard penetration test (SPT) and split-barrel sampling of soils Retrieved from https://www.astm.org/d1586_d1586m-18e01.html

Anderson, R. S., Anderson, S. P., & Tucker, G. E. (2013). Rock damage and regolith transport by frost: An example of climate modulation of the geomorphology of the critical zone. *Earth Surface Processes and Landforms*, *38*(3), 299–316. https://doi.org/10.1002/esp.3330

Anderson, R. S., Rajaram, H., & Anderson, S. P. (2019). Climate driven coevolution of weathering profiles and hillslope topography generates dramatic differences in critical zone architecture. *Hydrological Processes*, *33*(1), 4–19. https://doi.org/10.1002/hyp.13307

Anderson, S. P., Hinckley, E.-L., Kelly, P., & Langston, A. (2014). Variation in critical zone processes and architecture across slope aspects. *Procedia Earth and Planetary Science*, *10*, 28–33. https://doi.org/10.1016/j.proeps.2014.08.006

Atwater, T., & Stock, J. (1998). Pacific-North America plate tectonics of the Neogene southwestern United States: An update. *International Geology Review*, *40*(5), 375–402. https://doi.org/10.1080/00206819809465216

Bale, C. L., Williams, J. B., & Charley, J. L. (1998). The impact of aspect on forest structure and floristics in some Eastern Australian sites. *Forest Ecology and Management*, *110*(1–3), 363–377. https://doi.org/10.1016/s0378-1127(98)00300-4

Befus, K. M., Sheehan, A. F., Leopold, M., Anderson, S. P., & Anderson, R. S. (2011). Seismic constraints on critical zone architecture, Boulder Creek watershed, Front Range, Colorado. *Vadose Zone*, *10*(3), 915–927. https://doi.org/10.2136/vzj2010.0108

Blazevic, L. A., Bodet, L., Pasquet, S., Linde, N., Jougnot, D., & Longuevergne, L. (2020). Time-lapse seismic and electrical monitoring of the vadose zone during a controlled infiltration experiment at the Ploemeur hydrological observatory, France. *Water*, *12*(5), 1230. https://doi.org/10.3390/w12051230

Brantley, S. L., Lebedeva, M. I., Balashov, V. N., Singha, K., Sullivan, P. L., & Stinchcomb, G. (2017). Toward a conceptual model relating chemical reaction fronts to water flow paths in hills. *Geomorphology*, *277*, 100–117. https://doi.org/10.1016/j.geomorph.2016.09.027

Brooks, P. D., Chorover, J., Fan, Y., Godsey, S. E., Maxwell, R. M., McNamara, J. P., & Tague, C. (2015). Hydrological partitioning in the critical zone: Recent advances and opportunities for developing transferable understanding of water cycle dynamics. *Water Resources Research*, *51*(9), 6973–6987. https://doi.org/10.1002/2015WR017039

Burdick, S., & Lekic, V. (2017). Velocity variations and uncertainty from transdimensional P-wave tomography of North America. *Geophysical Journal International*, *209*(2), 1337–1351. https://doi.org/10.1093/gji/ggx091

Callahan, R. P., Riebe, C. S., Pasquet, S., Ferrier, K. L., Grana, D., Sklar, L. S., et al. (2020). Subsurface weathering revealed in hillslope-integrated porosity distributions. *Geophysical Research Letters*, *47*(15), e2020GL088322. https://doi.org/10.1029/2020gl088322

Callahan, R. P., Riebe, C. S., Sklar, L. S., Pasquet, S., Ferrier, K. L., Hahm, W. J., et al. (2022). Forest vulnerability to drought controlled by bedrock composition. *Nature Geoscience*, *15*(9), 1–6. https://doi.org/10.1038/s41561-022-01012-2

Chen, H., & Niu, Q. (2022). Improving moisture content estimation from field resistivity measurements with subsurface structure information. *Journal of Hydrology*, *613*, 128343. https://doi.org/10.1016/j.jhydrol.2022.128343

Clarke, B. A., & Burbank, D. W. (2011). Quantifying bedrock-fracture patterns within the shallow subsurface: Implications for rock mass strength, bedrock landslides, and erodibility. *Journal of Geophysical Research*, *116*(F4), F04009. https://doi.org/10.1029/2011JF001987

Cole, K. (1983). Late Pleistocene vegetation of kings canyon, Sierra Nevada, California. *Quaternary Research*, *19*(1), 117–129. https://doi.org/10.1016/0033-5894(83)90031-5

Dietrich, W. (2019). *High resolution mapping of antelope valley ranch, ca*. National Center for Airborne Laser Mapping (NCALM). https://doi.org/10.5069/G9QC01MQ

Donaldson, A. M., Zimmer, M., Huang, M.-H., Johnson, K., Hudson-Rasmussen, B., Finnegan, N., et al. (2023). Symmetry in hillslope steepness and saprolite thickness between hillslopes with opposing aspects. *Journal of Geophysical Research: Earth Surface*, *128*, e2023JF007076. https://doi.org/10.1029/2023JF007076

Dvorkin, J., Walls, J., & Davalos, G. (2021). Velocity-porosity-mineralogy model for unconventional shale and its applications to digital rock physics. *Frontiers in Earth Science*, *8*. https://doi.org/10.3389/feart.2020.613716

East, A. E., & Sankey, J. B. (2020). Geomorphic and sedimentary effects of modern climate change: Current and anticipated future conditions in the western United States. *Reviews of Geophysics*, *58*(4), e2019RG000692. https://doi.org/10.1029/2019RG000692

Eberhart-Phillips, D., Han, D.-H., & Zoback, M. D. (1989). Empirical relationships among seismic velocity, effective pressure, porosity, and clay content in sandstone. *Geophysics*, *54*(1), 82–89. https://doi.org/10.1190/1.1442580

Flinchum, B. A., Holbrook, W. S., & Carr, B. J. (2022). What do P-wave velocities tell us about the critical zone? *Frontiers in Water*, *3*. https://doi.org/10.3389/frwa.2021.772185

Flinchum, B. A., Holbrook, W. S., Grana, D., Parsekian, A. D., Carr, B. J., Hayes, J. L., & Jiao, J. (2018). Estimating the water holding capacity of the critical zone using near-surface geophysics. *Hydrological Processes*, *32*(22), 3308–3326. https://doi.org/10.1002/hyp.13260

Flinchum, B. A., Holbrook, W. S., Rempe, D., Moon, S., Riebe, C. S., Carr, B. J., et al. (2018). Critical zone structure under a granite ridge inferred from drilling and three-dimensional seismic refraction data. *Journal of Geophysical Research*, *123*(6), 1317–1343. https://doi.org/10.1029/2017jf004280

Godderis, Y., & Brantley, S. L. (2013). Earthcasting the future critical zone. *Elementa*, *1*. https://doi.org/10.12952/journal.elementa.000019

Grana, D., Parsekian, A. D., Flinchum, B. A., Callahan, R. P., Smeltz, N. Y., Li, A., et al. (2022). Geostatistical rock physics inversion for predicting the spatial distribution of porosity and saturation in the critical zone. *Mathematical Geosciences*, *54*(8), 1315–1345. https://doi.org/10.1007/s11004-022-10006-0

Gu, X., Mavko, G., Ma, L., Oakley, D., Accardo, N., Carr, B. J., et al. (2020). Seismic refraction tracks porosity generation and possible CO_2 production at depth under a headwater catchment. *Proceedings of the National Academy of Sciences of the United States of America*, *117*(32), 18991–18997. https://doi.org/10.1073/pnas.2003451117

Hahm, W. J., Dralle, D. N., Rempe, D. M., Bryk, A. B., Thompson, S. E., Dawson, T. E., & Dietrich, W. E. (2019). Low subsurface water storage capacity relative to annual rainfall decouples Mediterranean plant productivity and water use from rainfall variability. *Geophysical Research Letters*, *46*(12), 6544–6553. https://doi.org/10.1029/2019gl083294

Hahm, W. J., Dralle, D. N., Sanders, M., Bryk, A. B., Fauria, K. E., Huang, M.-H., et al. (2022). Bedrock vadose zone storage dynamics under extreme drought: Consequences for plant water availability, recharge, and runoff. *Water Resources Research*, *58*(4). https://doi.org/10.1029/2021WR031781

Hahm, W. J., Rempe, D. M., Dralle, D. N., Dawson, T. E., Lovill, S. M., Bryk, A. B., et al. (2019). Lithologically controlled subsurface critical zone thickness and water storage capacity determine regional plant community composition. *Water Resources Research*, *55*(4), 3028–3055. https://doi.org/10.1029/2018WR023760

Hahm, W. J., Riebe, C. S., Lukens, C. E., & Araki, S. (2014). Bedrock composition regulates mountain ecosystems and landscape evolution. *Proceedings of the National Academy of Sciences of the United States of America*, *111*(9), 3338–3343. https://doi.org/10.1073/pnas.1315667111

Handwerger, A. L., Huang, M.-H., Fielding, E. J., Booth, A. M., & Burgmann, R. (2019). A shift from drought to extreme rainfall drives a stable landslide to catastrophic failure. *Scientific Reports*, *9*(1), 1569. https://doi.org/10.1038/s41598-018-38300-0

Harwood, D. S., & Helley, E. J. (1987). Late Cenozoic tectonism of thhe Sacramento Valley, California. Profesisonal Paper 1359. https://doi.org/10.3133/pp1359

Hasenmueller, E. A., Gu, X., Weitzman, J. N., Adams, T. S., Stinchcomb, G. E., EissenstatKaye, D. M. J. P., & Brantley, S. L. (2017). Weathering of rock to regolith: The activity of deep roots in bedrock fractures. *Geoderma*, *300*, 11–31. https://doi.org/10.1016/j.geoderma.2017.03.020

Hayes, J. L., Riebe, C. S., Holbrook, W. S., Flinchum, B. A., & Hartsough, P. C. (2019). Porosity production in weathered rock: Where volumetric strain dominates over chemical mass loss. *Science Advances*, *5*(9). https://doi.org/10.1126/sciadv.aao0834

Helgerud, M. B., Dvorkin, J., Nur, A., Sakai, A., & Collett, T. (1999). Elastic-wave velocity in marine sediments with gas hydrates: Effective medium modeling. *Geophysical Research Letters*, *26*(13), 2021–2024. https://doi.org/10.1029/1999gl900421

Holbrook, W. S., Marcon, V., Bacon, A. R., Brantley, S. L., Carr, B. J., Flinchum, B. A., & Riebe, C. S. (2019). Links between physical and chemical weathering inferred from a 65-m-deep borehole through Earth's critical zone. *Scientific Reports*, *9*(1), 4495. https://doi.org/10.1038/s41598-019-40819-9

Holbrook, W. S., Riebe, C. S., Elwaseif, M., Hayes, J. L., Harry, D. L., Basler-Reeder, K., et al. (2014). Geophysical constraints on deep weathering and water storage potential in the Southern Sierra Critical Zone Observatory. *Earth Surface Processes and Landforms*, *39*(3), 366–380. https://doi.org/10.1002/esp.3502

Huang, M.-H., Hudson-Rasmussen, B., Burdick, S., Lekic, V., Nelson, M. D., Fauria, K. E., & Schmerr, N. (2021). Bayesian seismic refraction inversion for critical zone science and near-surface applications. *Geochemistry, Geophysics, Geosystems*, *22*(5), e2020GC009172. https://doi.org/10.1029/2020GC009172

Inbar, A., Nyman, P., Rengers, F. K., Lane, P. N. J., & Sheridan, G. J. (2018). Climate dictates magnitude of asymmetry in soil depth and hillslope gradient. *Geophysical Research Letters*, *45*(13), 6514–6522. https://doi.org/10.1029/2018gl077629

21699011, 2023, 7, Downloaded from https://agupubs.onlinelibrary.wiley.com/doi/10.1029/2023JF007254 by Test, Wiley Online Library on [03/07/2023]. See the Terms and Conditions (https://onlinelibrary.wiley.com/terms-and-conditions) on Wiley Online Library for rules of use; OA articles are governed by the applicable Creative Commons License

Istanbulluoglu, E., Yetemen, O., Vivoni, E. R., Gutiérrez-Jurado, H. A., & Bras, R. L. (2008). Eco-geomorphic implications of hillslope aspect: Inferences from analysis of landscape morphology in central New Mexico. *Geophysical Research Letters*, *35*(14), L14403. https://doi.org/10.1029/2008gl034477

Klos, P. Z., Goulden, M. L., Riebe, C. S., Tague, C. L., O'Geen, A. T., Flinchum, B. A., et al. (2018). Subsurface plant-accessible water in mountain ecosystems with a Mediterranean climate. *WIREs Water*, *5*(3). https://doi.org/10.1002/wat2.1277

Lebedeva, M. I., & Brantley, S. L. (2013). Exploring geochemical controls on weathering and erosion of convex hillslopes: Beyond the empirical regolith production function. *Earth Surface Processes and Landforms*, *38*(15), 1793–1807. https://doi.org/10.1002/esp.3424

Lebedeva, M. I., & Brantley, S. L. (2020). Relating the depth of the water table to the depth of weathering. *Earth Surface Processes and Landforms*, *45*(9), 2167–2178. https://doi.org/10.1002/esp.4873

Lee, S. G., & de Freitas, M. H. (1990). Seismic refraction surveys for predicting the intensity and depth of weathering and fracturing in granitic masses. *Field Testing in Engineering*, *6*(1), 241–256. https://doi.org/10.1144/gsl.eng.1990.006.01.27

Lee, S. S. (2018). Spatial Patterns of bedrock weathering at the hillslope scale inferred via drilling and multi-scale geophysical methods. (Master's Thesis). University of Texas.

Leone, J. D., Holbrook, W. S., Riebe, C. S., Chorover, J., Ferré, T. P. A., Carr, B. J., & Callahan, R. P. (2020). Strong slope-aspect control of regolith thickness by bedrock foliation. *Earth Surface Processes and Landforms*, *45*(12), 2998–3010. https://doi.org/10.1002/esp.4947

Mavko, M., Mukerji, T., & Dvorkin, J. (2009). *Appendices. The rock physics handbook: Tools for seismic analysis of porous media* (pp. 437–478). Cambridge University Press.

McGuire, L. A., Pelletier, J. D., & Roering, J. J. (2014). Development of topographic asymmetry: Insights from dated cinder cones in the western United States. *Journal of Geophysical Research: Earth Surface*, *119*(8), 1725–1750. https://doi.org/10.1002/2014JF003081

Moon, S., Perron, J. T., Martel, S. J., Holbrook, W. S., & St Clair, J. (2017). A model of three-dimensional topographic stresses with implications for bedrock fractures, surface processes, and landscape evolution. *Journal of Geophysical Research: Earth Surface*, *122*(4), 823–846. https://doi.org/10.1002/2016JF004155

Nelson, M. D., Bryk, A. B., Fauria, K., Huang, M.-H., & Dietrich, W. E. (2017). *Physical properties of shallow landslides and their role in landscape evolution investigated with ultrahigh-resolution lidar data and aerial imagery*. AGU fall meeting Abstracts.

Nielsen, T., Bradford, J., Holbrook, W. S., & Seyfried, M. (2021). The effect of aspect and elevation on critical zone architecture in the Reynolds Creek critical zone observatory: A seismic refraction study. *Frontiers in Water*, *3*, 670524.

Olona, J., Pulgar, J. A., Fernández-Viejo, G., López-Fernández, C., & González-Cortina, J. M. (2010). Weathering variations in a granitic massif and related geotechnical properties through seismic and electrical resistivity methods. *Near Surface Geophysics*, *8*(6), 585–599. https://doi.org/10.3997/1873-0604.2010043

Pasquet, S., Holbrook, W. S., Carr, B. J., & Sims, K. W. W. (2016). Geophysical imaging of shallow degassing in a Yellowstone hydrothermal system. *Geophysical Research Letters*, *43*(23), 12–027. https://doi.org/10.1002/2016gl071306

Pasquet, S., Marçais, J., Hayes, J. L., Sak, P. B., Ma, L., & Gaillardet, J. (2022). Catchment-scale architecture of the deep critical zone revealed by seismic imaging. *Geophysical Research Letters*, *49*(13), 12027–12035. https://doi.org/10.1029/2022gl098433

Pawlik, L., Phillips, J. D., & Samonil, P. (2016). Roots, rock, and regolith: Biomechanical and biochemical weathering by trees and its impact on hillslopes—A critical literature review. *Earth-Science Reviews*, *159*, 142–159. https://doi.org/10.1016/j.earscirev.2016.06.002

Pedrazas, M. A., Hahm, W. J., Huang, M.-H., Dralle, D., Nelson, M. D., Breunig, R. E., et al. (2021). The relationship between topography, bedrock weathering, and water storage across a sequence of ridges and valleys. *Journal of Geophysical Research: Earth Surface*, *126*(4), e2020JF005848. https://doi.org/10.1029/2020JF005848

Pelletier, J. D. (2017). Quantifying the controls on potential soil production rates: A case study of the San Gabriel Mountains, California. *Earth Surface Dynamics*, *5*(3), 479–492. https://doi.org/10.5194/esurf-5-479-2017

Pelletier, J. D., Barron-Gafford, G. A., Gutiérrez-Jurado, H., Hinckley, E. S., Istanbulluoglu, E., McGuire, L. A., et al. (2018). Which way do you lean? Using slope aspect variations to understand critical zone processes and feedbacks. *Earth Surface Processes and Landforms*, *43*(5), 1133–1154. https://doi.org/10.1002/esp.4306

Rempe, D. M., & Dietrich, W. E. (2014). A bottom-up control on fresh-bedrock topography under landscapes. *Proceedings of the National Academy of Sciences of the United States of America*, *111*(18), 6576–6581. https://doi.org/10.1073/pnas.1404763111

Rich, E. I. (1971). Geologic map of the Wilbur Springs quadrangle, Colusa and lake counties, California (Tech. Rep.).

Sanders, M., Nelson, M. D., Bryk, A. B., Huang, M.-H., Fauria, K., & Dietrich, W. E. (2019). The role of small shallow landslides in landscape evolution as revealed by high resolution differential lidar surveys and field mapping. In *AGU fall meeting 2019*. AGU.

Solazzi, S. G., Bodet, L., Holliger, K., & Jougnot, D. (2021). Surface-wave dispersion in partially saturated soils: The role of capillary forces. *Journal of Geophysical Research: Solid Earth*, *126*(12), e2021JB022074. https://doi.org/10.1029/2021jb022074

St Clair, J., Moon, S., Holbrook, W. S., Perron, J. T., Riebe, C. S., Martel, S. J., et al. (2015). Geophysical imaging reveals topographic stress control of bedrock weathering. *Science*, *350*(6260), 534–538. https://doi.org/10.1126/science.aab2210

Sullivan, P. L., Billings, S. A., Hirmas, D., Li, L., Zhang, X., Ziegler, S., et al. (2022). Embracing the dynamic nature of soil structure: A paradigm illuminating the role of life in critical zones of the Anthropocene. *Earth-Science Reviews*, *225*, 103873. https://doi.org/10.1016/j.earscirev.2021.103873

Wang, W., Nyblade, A. A., Mount, G., Moon, S., Chen, P., Accardo, N., et al. (2021). 3D seismic anatomy of a watershed reveals climate-topography coupling that drives water flowpaths and bedrock weathering. *Journal of Geophysical Research: Earth Surface*, *126*(12), e2021JF006281. https://doi.org/10.1029/2021JF006281

West, N., Kirby, E., Nyblade, A. A., & Brantley, S. L. (2019). Climate preconditions the critical zone: Elucidating the role of subsurface fractures in the evolution of asymmetric topography. *Earth Surface Processes and Landforms*, *513*, 197–205. https://doi.org/10.1016/j.epsl.2019.01.039

Xu, X., Sandwell, D. T., Klein, E., & Bock, Y. (2021). Integrated Sentinel-1 InSAR and GNSS time-series along the San Andreas Fault system. *Journal of Geophysical Research: Solid Earth*, *126*(11), e2021JB022579. https://doi.org/10.1029/2021JB022579

Zeng, Y., Petersen, M. D., & Shen, Z.-K. (2018). Earthquake potential in California-Nevada implied by correlation of strain rate and seismicity. *Geophysical Research Letters*, *45*(4), 1778–1785. https://doi.org/10.1002/2017GL075967

21699011, 2023, 7, Downloaded from https://agupubs.onlinelibrary.wiley.com/doi/10.1029/2023JF007254 by Test, Wiley Online Library on [03/07/2023]. See the Terms and Conditions (https://onlinelibrary.wiley.com/terms-and-conditions) on Wiley Online Library for rules of use; OA articles are governed by the applicable Creative Commons License